



**HAL**  
open science

# A four-dimensional mesoscale map of the spring bloom in the northeast Atlantic (POMME experiment): Results of a prognostic model

Marina Lévy, M. Gavart, Laurent Mémery, Guy Caniaux, A. Paci

## ► To cite this version:

Marina Lévy, M. Gavart, Laurent Mémery, Guy Caniaux, A. Paci. A four-dimensional mesoscale map of the spring bloom in the northeast Atlantic (POMME experiment): Results of a prognostic model. *Journal of Geophysical Research*, 2005, 110, pp.C07S21. 10.1029/2004JC002588 . hal-00124671

**HAL Id: hal-00124671**

**<https://hal.science/hal-00124671>**

Submitted on 1 Mar 2021

**HAL** is a multi-disciplinary open access archive for the deposit and dissemination of scientific research documents, whether they are published or not. The documents may come from teaching and research institutions in France or abroad, or from public or private research centers.

L'archive ouverte pluridisciplinaire **HAL**, est destinée au dépôt et à la diffusion de documents scientifiques de niveau recherche, publiés ou non, émanant des établissements d'enseignement et de recherche français ou étrangers, des laboratoires publics ou privés.

## A four-dimensional mesoscale map of the spring bloom in the northeast Atlantic (POMME experiment): Results of a prognostic model

M. Lévy,<sup>1</sup> M. Gavart,<sup>2</sup> L. Mémerly,<sup>3</sup> G. Caniaux,<sup>4</sup> and A. Paci<sup>4</sup>

Received 13 July 2004; revised 15 November 2004; accepted 4 January 2005; published 15 June 2005.

[1] A prognostic high-resolution model is established to provide an integrated view of the evolution of the spring bloom during the Programme Océan Multidisciplinaire Méso Echelle (POMME) experiments carried out at sea from February to May 2001 (16–22°W and 38°–45°N). Data collected during the first survey were used for model initialization, and data from three other cruises were used for model validation. The model successfully predicts the time evolution of the main reservoirs and fluxes, except for a storm event during postbloom conditions, for which the biological impact is underestimated. The bloom is long in duration (2 months), has low intensity (1 mg Chl m<sup>-3</sup>), and is characterized by a small *f*-ratio (0.45) and a small *e*-ratio (0.05). Furthermore, the model reveals much stronger space and time variability than sampled in the data. This large variability results both from the synoptic atmospheric variability and from the stirring induced by oceanic mesoscale eddies. In particular, the bloom starts in specific submesoscale features that correspond to filaments of minimum mixed layer depth. On short timescales (2–3 days), space and time variability have the same order of magnitude. On the seasonal timescale, time variability is larger than space variability. Considering the transient state of the system, this modeling exercise is also used to quantify the nonsynopticity of the observations, which occur mostly during bloom conditions, a crucial point for the data interpretation.

**Citation:** Lévy, M., M. Gavart, L. Mémerly, G. Caniaux, and A. Paci (2005), A four-dimensional mesoscale map of the spring bloom in the northeast Atlantic (POMME experiment): Results of a prognostic model, *J. Geophys. Res.*, 110, C07S21, doi:10.1029/2004JC002588.

### 1. Introduction

[2] The meridional gradient in winter mixed layer depth (MLD) divides the northeast Atlantic into two regions, a rather productive one to the north, associated with the deepest mixed layers (ML), and a more oligotrophic one to the south [Lévy *et al.*, 2005]. Combined with a mean geostrophic southward motion, this sharp southward decrease of the winter MLD also explains the subduction of subpolar mode water [Paillet and Arhan, 1996a, 1996b].

[3] In 2001, the Programme Océan Multidisciplinaire Méso Echelle (POMME) staged a coordinated multidisciplinary effort at sea to investigate the subduction mechanisms of subpolar mode water in the northeast Atlantic, how this affects the biological production and the carbon budget,

and to describe the fate of organic matter after subduction [Mémerly *et al.*, 2005]. These issues are crucial in the context of the oceanic carbon cycle, because the area is a strong sink of atmospheric CO<sub>2</sub> [Rios *et al.*, 1995] and because the subducted waters are isolated on decadal timescales from the influence of the atmosphere [McCartney and Talley, 1982; Jenkins, 1998]. Moreover, as subduction and the spring bloom occurs at the same period, at the end of winter when the mixed layer retreats, it is important to understand the timing of these two processes: primary productivity drives the biogeochemical properties of the water masses before they are subducted into the main thermocline.

[4] POMME was conducted with strong emphasis on the role of mesoscale eddies. Indeed, a decade before POMME, the North Atlantic Bloom Experiment (NABE) revealed the importance of the connections between the upper ocean mesoscale variability and the biological signals of the spring bloom in the northeast Atlantic [Robinson *et al.*, 1993; Yoder *et al.*, 1993; McGillicuddy *et al.*, 1995a, 1995b]. The emphasis on mesoscale structures also stems from numerical studies, which suggest that eddies are important contributors to both the subduction [Hazeleger and Drijfhout, 2000; Valdivieso Da Costa *et al.*, 2005] and the production budgets [McGillicuddy *et al.*, 1995b; Oschlies and Garçon,

<sup>1</sup>Laboratoire d'Océanographie Dynamique et de Climatologie/Institut Pierre-Simon Laplace, CNRS, Paris, France.

<sup>2</sup>Service Hydrographique et Océanographique de la Marine, Toulouse, France.

<sup>3</sup>Laboratoire des Sciences de l'Environnement, CNRS, UMR 6539, Institut Universitaire Européen de la Mer, Plouzané France.

<sup>4</sup>Centre National de Recherches Meteorologiques, Meteo-France, Toulouse, France.

1998; *McGillicuddy et al.*, 1998; *Mahadevan and Archer*, 2000; *Lévy et al.*, 2001].

[5] Data gathered during mesoscale surveys are generally asymptotic [*McGillicuddy et al.*, 2001; *Anderson and Robinson*, 2001; *Popova et al.*, 2002], particularly during transient regimes. Discerning the effects of temporal and spatial variations is a difficult exercise, and coupled biological and physical modeling has proven an effective tool in providing temporal structures consistent with physical and biological conditions [*McGillicuddy et al.*, 1995b; *Anderson and Robinson*, 2001; *Franks and Chen*, 2001; *Popova et al.*, 2002]. This paper is in the line of such approaches. The domain of the POMME surveys covers 7° in latitude and 6° in longitude (16°–22°W, 38°–45°N), and the sampling period examined in this paper extends from 2 February until 3 May 2001. In comparison with the above mentioned studies, the POMME domain is larger in space and time, at the expense of space and time resolution.

[6] A prognostic model is established to follow synoptically the evolution of the spring bloom during the winter (P1) and spring (P2) POMME cruises. The model is a high-resolution hydrodynamical regional model with open boundaries [*Gavart et al.*, 1999], coupled with a six-compartment biogeochemical model of the nitrogen cycle [*Lévy et al.*, 2001]. The model is initialized using the data from the first leg of P1 (P1L1), and is validated using data of P1L2, P2L1 and P2L2. A careful validation of the model dynamics and thermodynamics is presented by *Paci et al.* [2005]. The objective of this study is twofold. First, we intend to synthesize the information of the POMME biogeochemical data set of the euphotic layer, to put the observations back in the highly variable 4-D context, and to make the best reconstruction of the physical-biological state during the P1 and P2 cruises. Second, we intend, from this reconstruction, to improve our comprehension of the spring bloom in the northeast Atlantic, and in particular to derive regional budgets of production and export, and to quantify the different scales of variability of the physical and biological fields: the intraseasonal variability, the large-scale meridional gradient that results from the north south variation in MLD, and the submesoscale variability that results from the stirring associated with mesoscale eddies and interactions among them.

## 2. Programme Océan Multidisciplinaire Méso Echelle (POMME) Surveys

### 2.1. Observational Strategy and Asynopticity Problem

[7] As part of POMME, two oceanic cruises (P1 and P2) took place in winter and spring 2001 (Figure 1 and Table 1), each one divided in two legs (L1 and L2). The aim of P1 was to describe the winter conditions in order to estimate the maximum MLD and set initial prebloom conditions. The spring cruise P2 immediately followed, with the objective of characterizing the mode water subduction and the bloom evolution. The first legs were dedicated to a large-scale survey of the area. The main study area (39–44.5, 16°–21°W) was covered by seven latitudinal transects (R/V *l'Atalante*), with conductivity-temperature-depth (CTD) stations approximately 50 km apart and XBT (Expendable Bathythermograph) drops performed between CTD casts. In parallel, a second research vessel (R/V *D'Entrecasteaux*)

extended the observation area to 38°N in the South, 45°N in the north and 22°W in the west. The mesoscale flow field in the vicinity of the experiment was defined in near-real-time with an objective mapping scheme incorporating velocity and density data [*Assenbaum and Reverdin*, 2005], and with the North Atlantic operational forecasting system SOPRANE which is based on a quasi-geostrophic model incorporating altimetry [*Blayo et al.*, 1994]. During the second legs, four time series stations were carried for investigating one-dimensional (1-D) biogeochemical processes. They usually lasted 2 days.

[8] Ideally, the P1L1 and P2L1 data sets are meant to provide a global description of the area at two different periods, 1.5 months apart. A major decision in the POMME observational strategy concerned the necessary compromise between the extension of the surveyed area, the space resolution of the L1 arrays, and the time required to do the survey. The choice of the domain extension was constrained by the requirement to cover the meridional winter MLD gradient and to encompass a sufficient number of identified mesoscale structures. The drawback of this large model extension is that the distance between CTD casts (50 km) is not sufficient to precisely describe the mesoscale variability. Another shortcoming is that the array is covered in 3 weeks, which causes strong asynopticity in the data, because this duration is long compared to the characteristic timescale of the weather, the MLD, the ecosystem, and the eddy interactions. The second legs were designed to gain better insight on the mesoscale variability. The time series stations were located in specific regions of the mesoscale field using maps obtained with the quasi real time assimilation in the SOPRANE model. One difficulty in the interpretation of L2 data is again to disentangle between time and space variations of the observational data.

[9] The three legs P1L2, P2L1 and P2L2 were examined with a physical-biological model of the upper ocean (Appendix A), initialized on P1L1. The goal is to simulate the evolution of the POMME region during P1 and P2, using P1L1 data for initialization, but with a much higher horizontal resolution than the observations. Model results are then compared with observations taken during the three other legs, which in turn are put back in a more complete high-resolution 4-D context.

### 2.2. Measurements

[10] The various data sets used in this work were provided through the POMME database. We will discuss only those data used for initialization and comparison with the model run. On board the R/V *l'Atalante*, a Neil Brown CTD was used to collect conductivity and temperature profiles, most often associated with LADCP current profilers. A rosette of Niskin bottles was used to collect water samples to measure a set of core parameters. Nitrate and ammonium were measured with an autoanalyser [*Fernandez et al.*, 2005b]. Chlorophyll a was estimated by HPLC analysis [*Claustre et al.*, 2005]. New and regenerated production was measured using <sup>15</sup>N incubation techniques [*Fernandez et al.*, 2005a; S. Lhelguen et al., personal communication, 2004]. New production (NP) is referred in this paper as the production based on nitrate consumption. Regenerated production (RP) is referred as the assimilation of ammonium (plus urea,

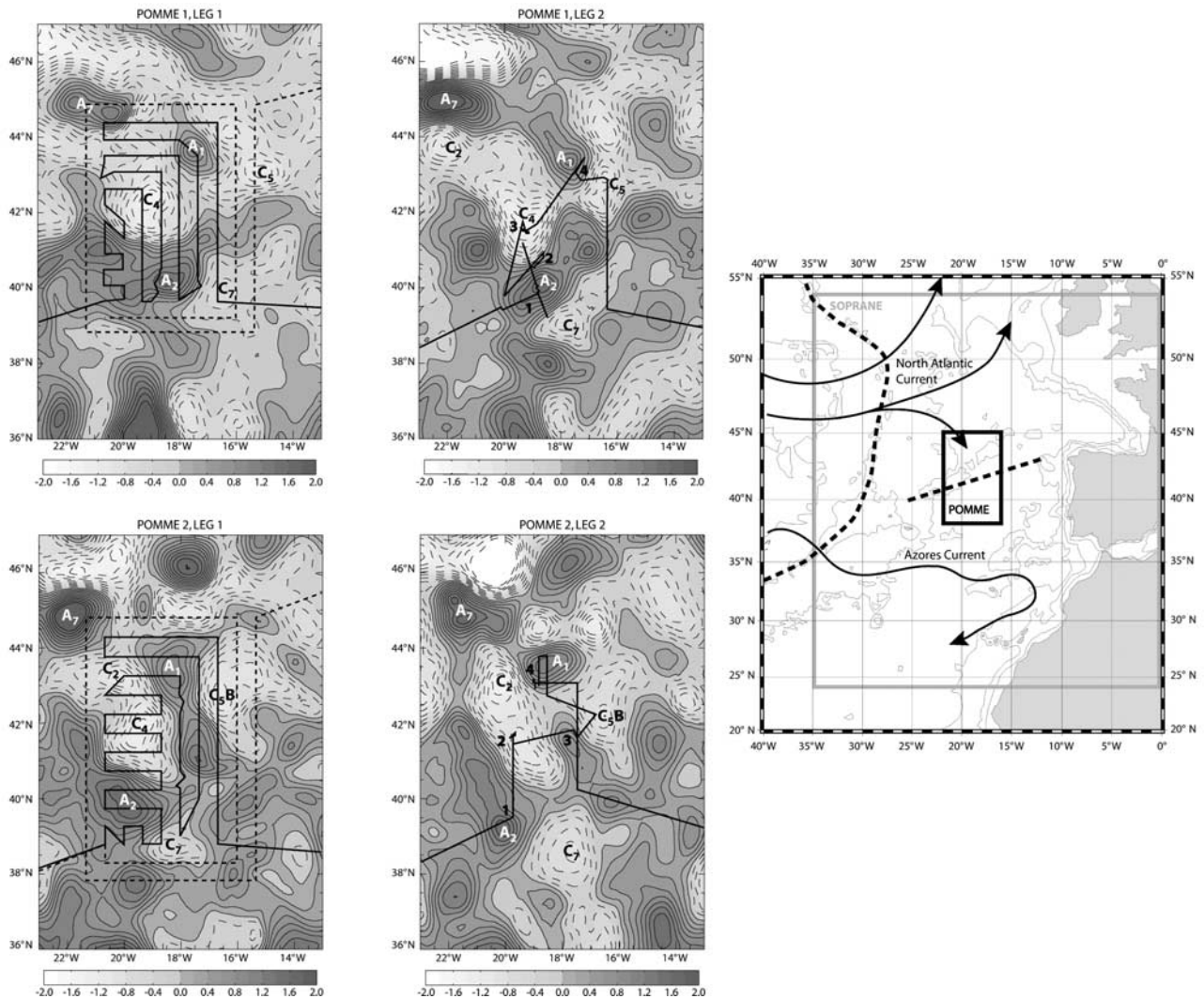


**Figure 1.** Maps of the Programme Océan Multidisciplinaire Méso Echelle (POMME) area and of cruise tracks of the R/V *l'Atalante* (solid lines) and R/V *D'Entrecasteaux* (dotted lines) during each leg of P1 and P2, superimposed on the mesoscale field (stream functions in  $\text{cm}^2 \text{s}^{-1}$ ) estimated in near-real-time [Assenbaum and Reverdin, 2005]. Identified cyclones (C), anticyclones (A), and time series stations (1–4) of legs 2 are also indicated. On the large-scale view the main currents (black arrows), the approximate location of the MLD largest gradient (dotted line), and the POMME and the SOPRANE domains are indicated.

when measured). The  $f$ -ratio is referred as  $\text{NP}/(\text{NP} + \text{RP})$ , without correcting for nitrification or vertical transport of ammonium.

[11] Drifting sediment trap moorings (at 200 m and 400 m) were deployed at the L2 stations (N. Leblond, personal communication, 2004). The  $e$ -ratio is defined as the sediment trap flux at 200 m divided by the total production ( $\text{NP} + \text{RP}$ ). Zooplankton was measured at L2 stations, which includes mesozooplankton measured by WP2 nets (V. Andersen et al., personal communication, 2004), ciliates [Karayanni et al., 2005a] and heterotrophic nanoflagellates [Karayanni et al., 2005b]. WP2 data was converted to nitrogen using a ratio of  $1 \text{ mg m}^{-3}$  dry weight to  $0.1 \text{ mgN m}^{-3}$ . Ciliates and flagellates were measured in carbon and converted to nitrogen using a C:N ratio of 4 and 6.6, respectively. Total organic nitrogen (TON) was measured by P. Raimbault (personal communication, 2004). Semilabile DON was assumed to be

a fraction (40% (R. Sempéré, personal communication, 2004)) of TON.

### 2.3. Overview of P1L1 (Model Initial State)

[12] Figure 2 shows the cyclonic (C2, C4, C5, C6, C7) and anticyclonic (A1, A2, A4, A5, A7) structures that have been identified during P1 and P2 [Assenbaum and Reverdin, 2005]. Hydrographic measurements reveal that A2 and C4

**Table 1.** Schedule of Programme Océan Multidisciplinaire Méso Echelle (POMME) Winter and Spring Legs

	Begin Date	End Date
P1L1	3 Feb. 2001	23 Feb. 2001
P1L2	28 Feb. 2001	19 March 2001
P2L1	24 March 2001	12 April 2001
P2L2	17 April 2001	3 May 2001

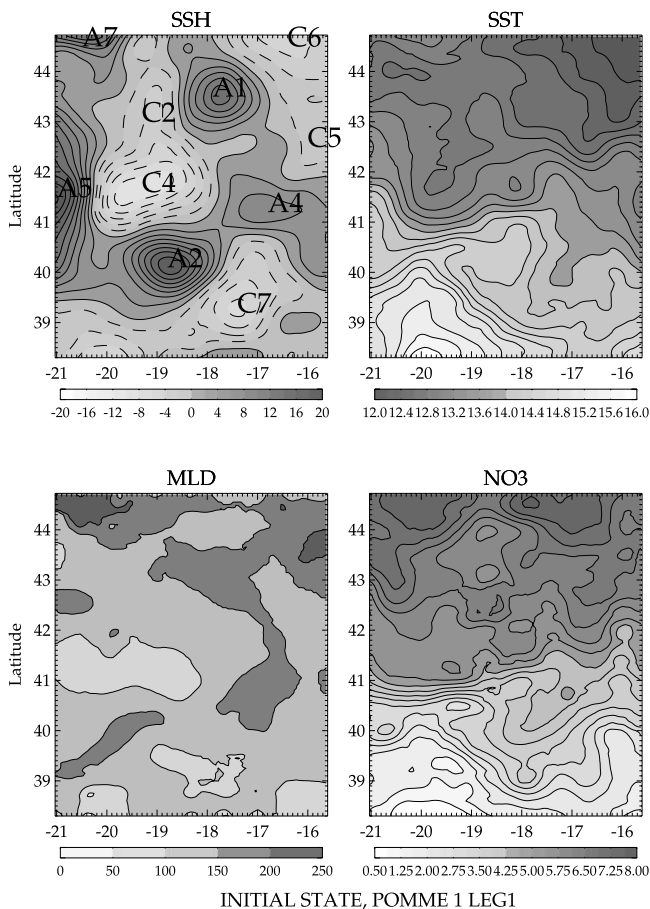


**Figure 2.** Sea surface height (SSH) (in centimeters, contours every 2 cm), sea surface temperature (SST) (in degrees Celsius, contours every  $0.2^\circ$ ), mixed layer depth (MLD) (in meters, contours every 50 m), and surface nitrate concentration ( $\text{NO}_3$ ) (in  $\text{mmolN m}^{-3}$ , contours  $0.375 \text{ mmolN m}^{-3}$ ) during PIL1 used to initialize the model. Cyclones and anticyclones are identified on the SSH plot, following the naming convention of Figure 1.

are surface intensified, and associated with warm and cold surface anomalies, respectively. A1 is a mode water eddy, particularly intense at middepth and with no sea surface temperature (SST) signal.

[13] Best estimates of temperature and salinity for PIL1 were obtained as follows. First, individual profiles have been aged. Aging consists of integrating each profile with a 1-D turbulent model from the actual date of the measurement until the last day of PIL1. This correction greatly improves the coherence between the hydrological fields, the ML and the air-sea fluxes, although it neglects the effect of advection. Incidentally, this correction was found to slightly decrease the correlation between observed and simulated horizontal fields, and was therefore not used by *Paci et al.* [2005]. Interpolation to the model grid is performed from objective analysis of the individual profiles, with an influence radius of 50 km as described by *Paci et al.* [2005]. A second correction is then applied, which consists of lowering/lifting the density surfaces to best fit the satellite SLA estimate during PIL1 [*Gavart et al.*, 1999]. This corrects the representation of the initial mesoscale structures. The

resulting SST field displays at approximately  $41^\circ\text{N}$  a frontal area between different water masses (colder and fresher waters to the north). On its western edge, the front corresponds to the boundary between A2 and C4.

[14] A variety of criteria has been proposed for the determination of the MLD during POMME. In this paper, it has been chosen as the density layer within  $0.01 \text{ kg m}^{-3}$  of the surface density. This criteria is the one that best represents winter conditions (L. Prieur, personal communication, 2004). The MLD during PIL1 is deeper in the north (between 150 and 250 m) than in the south (between 0 and 150 m). The deepest MLDs (250 m) are found in the north western corner of the domain.

[15] Geostrophic currents were deduced from this density field. These currents show good agreement with VM-ADCP measurements [*Paci et al.*, 2005]. The 1800 m velocity field estimated by inversion of the data with a Kalman filter (F. Gaillard, personal communication, 2004) is chosen as the reference for the computation of geostrophic currents. Compared to the zero-velocity reference, this choice enhances the barotropic circulation, and leads to higher and more realistic kinetic energy in the model ( $66 \pm 3 \text{ cm}^2 \text{ s}^{-2}$  for a model run with zero-velocity reference level,  $86 \pm 1 \text{ cm}^2 \text{ s}^{-2}$  for a run with a 1800 m velocity reference, compared to  $89 \pm 6 \text{ cm}^2 \text{ s}^{-2}$  estimated from the data analysis of *Assenbaum and Reverdin* [2005]).

[16] The initial state for nitrate was constructed from optimal interpolation of the profiles acquired during PIL1 on the model grid, with an influence radius of 50 km. Unlike for temperature and salinity, we have not attempted to correct for asynopticity in the nitrate data. A posteriori, this assumption rests on the observation that the nitrate concentration evolved very slowly until the beginning of March (see next paragraph). A nitrate front is associated with the temperature front. Surface nitrate concentrations range from  $4 \text{ mmolN m}^{-3}$  to the south to  $5\text{--}7 \text{ mmolN m}^{-3}$  to the north.

[17] The optimal interpolation of PIL1 Chla data and the Sea-viewing Wide Field-of-view Sensor (SeaWiFS) composite for the same period reveals patchy spatial structures that are not well correlated (not shown). This reflects the rapid timescale of phytoplankton evolution, which can double its biomass in 2 days in favorable conditions. In order to avoid introducing spurious variability in the model, we have chosen to homogeneously initialize phytoplankton. The mean PIL1 Chla profile is initially set throughout the domain. The other biological variables were distributed with the same profile (with an  $e$ -folding depth of 70 m). Initial surface values were established from PIL1 observations (Table 2). This hypothesis in the initialization cancels out a possible source of variability, that would come from large or mesoscale variations in the winter preconditioning.

**Table 2.** Surface Initial Values of the Model Biological Variables<sup>a</sup>

Variables	Values, $\text{mmol N m}^{-3}$
Phytoplankton	0.45
Zooplankton	0.15
Ammonium	0.06
Detritus	0.05
DOM	3.0

<sup>a</sup>These values are an average of PIL1 surface data.

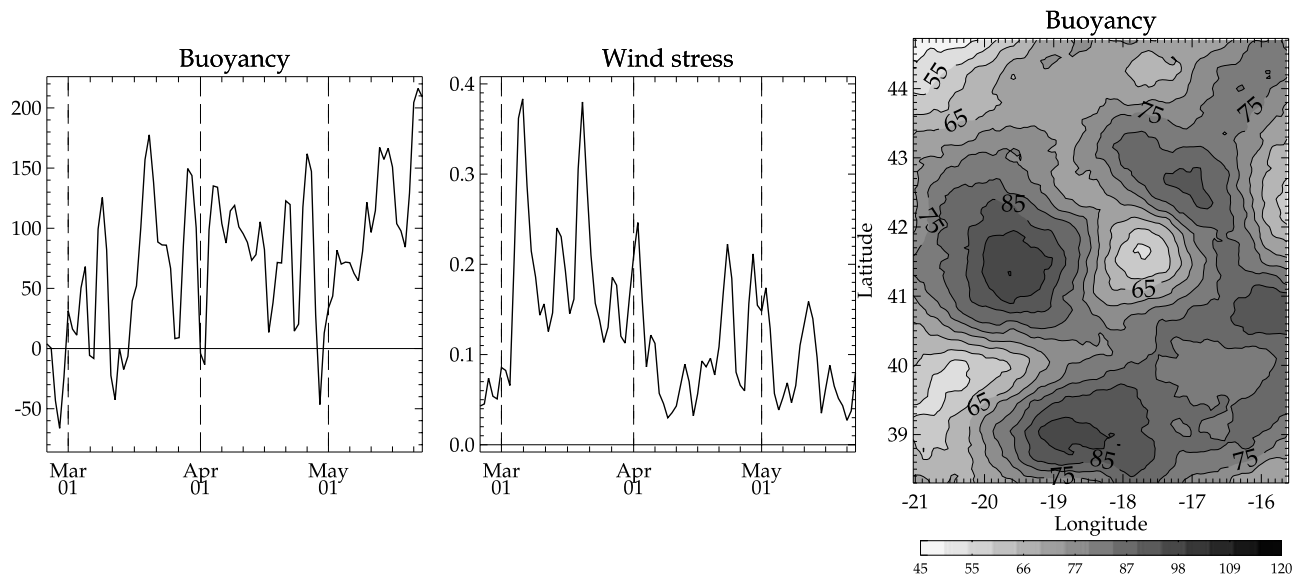


**Figure 3.** Atmospheric fluxes used to force the model. (left) Time evolution of buoyancy (defined in  $W m^{-2}$ ), averaged over the inside model domain. (middle) Time evolution of the wind stress module (in  $N m^{-2}$ ), averaged over the inside model domain. (right) Averaged buoyancy flux during the 3 months of the experiment.

Although some observations (pigment distributions with HPLC data, particulate and zooplankton stocks with HIAC and OPCT observations (A. Sciandra, personal communication, 2004; P. Labat, personal communication, 2004) suggest that this variability might exist, clearly not enough information is available to properly constrain it. Owing to vertical mixing, the initial profiles of biogeochemical tracers are rapidly (1 day) homogenized within the mixed layer. This induces variability of the biogeochemical tracers initial surface values (in phase with the MLD variability), but not of their depth integrated value.

#### 2.4. Overview of the Atmospheric Forcings

[18] Shipboard records of meteorological parameters, combined with satellite estimates, weather prediction model outputs and specific state-of-the-art bulk formulae deduced from turbulence measurements performed on board the R/V *l'Atalante* were used to estimate daily surface forcing at the resolution of the oceanic mesoscale [Caniaux *et al.*, 2005]. Observed heat and salt budgets were used to constrain the adjustment of the fluxes. The surface is forced with these daily estimates of penetrative solar radiation, net radiative and turbulent heat fluxes (sensible plus latent), evaporation minus precipitation, and wind stress.

[19] Figure 3 shows the records of wind stress and buoyancy flux averaged over the domain. Buoyancy is defined in  $W m^{-2}$  as  $B = Q - empC_p(\beta/\alpha)S$ , with  $Q$  the total net heat flux,  $C_p$  the calorific capacity of seawater,  $\alpha$  the thermal expansion,  $\beta$  the salinity expansion,  $S$  the salinity, and  $emp$  the evaporation minus precipitation budget. On the seasonal timescale, buoyancy switches from negative to positive values. This switch roughly occurs around the first of March. However, strong wind events in March and April occasionally cause large buoyancy variations on short timescales. An atmospheric depression also passed through the area later in the season (23 April–2 May), during P2L2.

[20] Reconstruction of the atmospheric forcing with high resolution enabled to witness space anomalies in the buoyancy forcing. These anomalies are in fact the fingerprint of the oceanic mesoscale eddies. They persist over a season (Figure 3) because of the slow evolution of the eddies (Figure 1). Particularly obvious are the larger buoyancy gains over cyclones C4 and C7, due to their cold SST anomalies [Bourras *et al.*, 2004].

### 3. Models

#### 3.1. Physical Model

##### 3.1.1. Model Domain

[21] The ocean circulation model OPA [Madec *et al.*, 1999] (available at <http://www.lodyc.jussieu.fr/NEMO>) is used. The domain geometry is a rectangle on the sphere with open boundaries and realistic topography. The resolution is 1/20 of a degree on the horizontal. There are 69  $z$  coordinate vertical layers, with 5 m resolution in the upper 150 m. An open domain is embedded inside a closed domain and separated from it by a sponge zone (Figure 4) [Gavart *et al.*, 1999]. Open boundary heat and salt fluxes are constrained by the R/V *D'Entrecasteaux* hydrographic data. A linear temporal interpolation is used between P1L1 and P2L1 boundary data, while the boundary condition is kept constant after P2L1. Preliminary experiments have shown that, over the timescale of the bloom, the evolution of the eddy field and MLD in the open domain are primarily constrained by the initial state and the atmospheric forcing, respectively, and only marginally sensitive to variations at the boundaries. Further details on the model configuration are given by Gavart *et al.* [1999] and Paci *et al.* [2005]. Model simulations start on 23 February and last 3 months.

##### 3.1.2. Model Physics

[22] Vertical eddy coefficients are computed from an embedded 1.5 turbulent closure model based on a prognos-

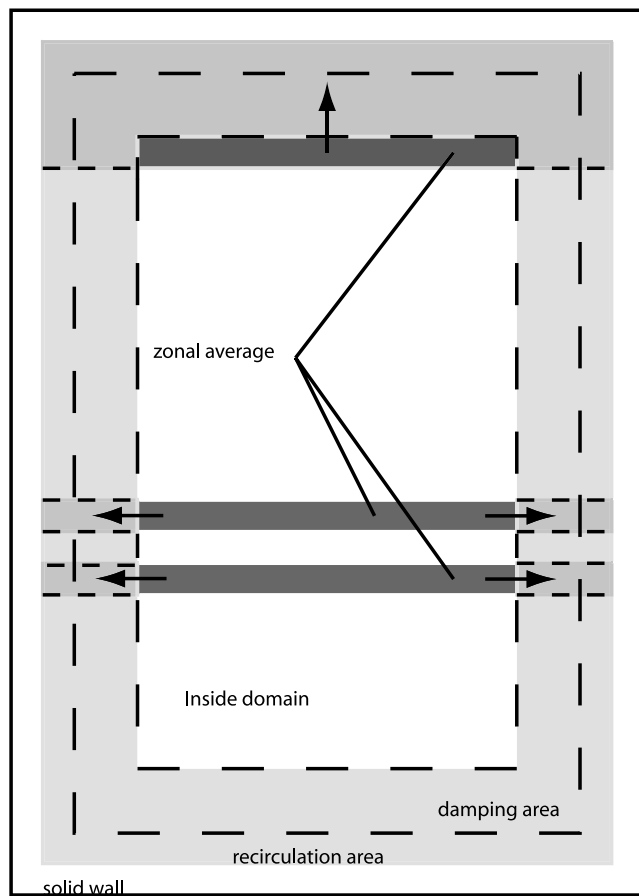


**Figure 4.** Schematic of the model domain and of its open boundary (dashed line). The damping area is shaded, and there is a recirculation area between the open boundary and the solid wall (see *Gavart et al.* [1999] for more details). The arrows and darker shading illustrate how the biological information in the inside domain is used to define the boundary conditions in the damping area.

tic equation of turbulent kinetic energy and a closure assumption for turbulent length scales [*Gaspar et al.*, 1990], and are enhanced in the case of convection. Horizontal mixing of density and momentum is included through biharmonic friction terms, with a dissipation coefficient  $|K_H| = 1.5 \times 10^9 \text{ m}^4 \text{ s}^{-1}$ .  $K_H$  was tuned to avoid numerical noise in the vertical velocity field. Results of a simulation with a resolution of 0.025 degree (approximately 2.5 km) and  $|K_H| = 0.5 \times 10^9 \text{ m}^4 \text{ s}^{-1}$  showed only marginal differences with the standard run (in comparison to the large differences obtained by *Lévy et al.* [2001] between 6 km and 2 km resolution runs). This is probably due to the fact that the eddy kinetic energy in POMME is less than in areas in the vicinity of strong currents which were dominant in *Lévy et al.*'s [2001] study. The time step is 5 min and model outputs are daily averages.

### 3.2. Biological Model

[23] We use the Lodyc Ocean Biogeochemical Simulation Tools for Ecosystem and Resources (LOBSTER) nitrogen-based biological model (Appendix A). This model contains six prognostic variables (nitrate, ammonium, phytoplankton,

zooplankton, detritus and semilabile dissolved organic matter).

[24] Fluxes of biogeochemical tracers at the model boundaries are not sufficiently constrained by the available data to be properly accounted for, particularly because of the rapid evolution during P2L1. Therefore the treatment of the open boundaries for biogeochemical tracers is set to minimize the impact of the boundaries on the interior evolution. This essentially amounts to neglecting the large-scale Ekman transport from the north [*Williams and Follows*, 1998], which is a reasonable assumption for a 3 month simulation, but would not hold for longer runs. Open boundaries for biogeochemical tracers are treated the same way as for temperature and salinity. Within a recirculating area surrounding the domain, tracers are restored toward a prescribed boundary value. It is the choice of these boundary values (BV) that enables control (and minimization) of the boundary fluxes. Until 4 April (i.e., before nitrate consumption rapidly accelerates in the model), the north and south nitrate BV are obtained from the linear interpolation in time between the R/V *D'Entrecasteaux* data of P1L1 and P2L1. After 4 April, in order to avoid spurious nitrate inputs (linear interpolation cannot account for the rapid consumption), nitrate BV are taken equal to the zonal average of nitrate along the boundary within the model domain (Figure 4). This technique to obtain north and south BV is applied to the other biogeochemical tracers during the whole course of the experiments, whereas the east and west BV are set equal to the zonal average within the domain.

## 4. Model Results

### 4.1. Time Variability and Comparison With Data

[25] In the following, data and model results are presented in a 1-D (time) view (Figures 5 and 6).

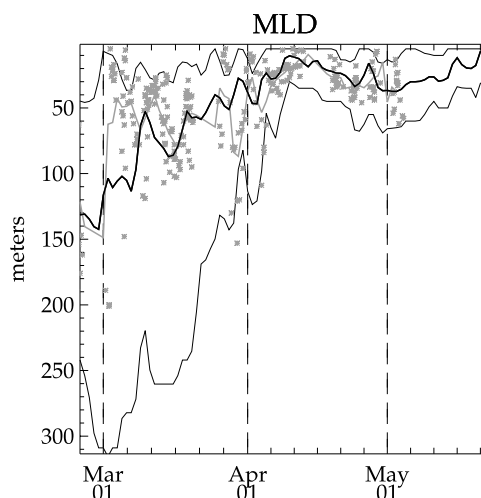


**Figure 5.** Comparison of the model MLD with the MLD estimated from conductivity-temperature-depth (CTD) casts. The bold line shows the time evolution of the model MLD, averaged over the model domain. The thin lines show the model minimum and maximum bounds. Shaded crosses are the MLD estimated from individual CTD casts. The shaded curve shows the result of a time filter applied over these data, with a 3 day window.

#### 4.1.1. Mixed Layer Depth

[26] The averaged MLD in the model reaches its deepest value (140 m) around 1 March (beginning of P1L2), right before the averaged buoyancy flux changes sign. Then, the ML progressively shallows and reaches a minimum of 10 m on 10 April. Owing to stormy atmospheric conditions during March, this 6 weeks retreat is interrupted on many occasions (10 March and 1 April being the largest events). The MLD remains rather shallow in April (10–30 m), and deepens again during the P2L2 storm (40 m on average). The large range between the maximum and minimum MLD values in March originates from the north-south winter MLD gradient, as well as from smaller-scale variability (see below).

[27] The MLD general evolution in the model agrees well with the observations. This can be verified by comparing the black curve on Figure 5 (the model spatial mean), with the grey curve (3 days running average over MLD estimates from individual CTD casts). Although the two curves represent different quantities (time/space average), they both indicate a rather slow MLD retreat, and comparable MLD magnitudes. More quantitative validation of the MLD at L2 time series stations is presented in the discussion. In Paci et al. (this issue), the SST and the temperature at 200 m depth are validated against L1 CTD data.

#### 4.1.2. Biogeochemical Stocks and Fluxes

[28] Surface Chla in the model shows only marginal evolution during P1L2 and P2L1, with average values around  $0.7 \text{ mgChl m}^{-3}$  (Figure 6). It starts increasing during the second part of P2L1, and peaks around 10 April. The peak value is  $1.1 \text{ mgChl m}^{-3}$  on average (with a local maxima of  $2.3 \text{ mgChl m}^{-3}$ ). Surface Chla decreases during P2L2. When integrated over the euphotic layer, the Chla content shows a slow decrease between P1L2 and P2L1, followed by a small increase during P2L2. Nitrate remains approximately constant during P1L2, and starts significantly decreasing during the second half of P2L1. It is locally exhausted by 10 April. NP approximately doubles between P1L2 and P2L1. On average, values over  $5 \text{ mmolN m}^{-2} \text{ d}^{-1}$  are sustained for over a month. Large day to day variability is observed, whose amplitude is similar to the seasonal amplitude. Note for instance the decrease between 30 March and 3 April, from  $5.5$  to  $3.5 \text{ mmolN m}^{-2} \text{ d}^{-1}$ . Comparatively, RP shows less seasonal variations (but similar daily variability), and averages  $4 \text{ mmolN m}^{-2} \text{ d}^{-1}$  during this winter-spring period. An exception is a significant increase during P2L2. The  $f$ -ratio (nitrate uptake divided by total production) ranges between 0.4 and 0.6. The integrated zooplankton increases between P1L2 and P2L1, and peaks at the end of P2L1. Sedimentation at 200 m follows the same trend. The  $e$ -ratio (sedimentation at 200 m divided by total production) is less than 5%. Note that the  $f$ -ratio and  $e$ -ratio in the model and in the data are computed with the same definitions. The model  $e$ -ratio is computed with for a reference level of 200 m instead of the more commonly used euphotic layer depth in order to allow direct comparison with the experimental  $e$ -ratio which is derived from 200 m sediment trap data.

[29] The overall agreement with the P1L2 and P2L1 observations is very satisfactory. During P1L2, surface and integrated Chla, nitrate, NP, RP and exported production,  $f$ -ratio and  $e$ -ratio in the model are in the range of the

observations reported at the time series stations. The general evolution of nitrate and Chla between P1L2 and P2L1 is well reproduced by the model, in particular for the stable values of Chla at the surface, the decrease in integrated Chla, and the decrease in nitrate. The difference in magnitude between the maximum and minimum values is also well captured by the model. Moreover, the model suggests a significant decrease in nitrate and integrated Chla during P2L1. The accuracy of this trend is confirmed by averaging the data over two boxes (in space) that were respectively sampled during the first and second part of the survey. An increase of a factor close to two is predicted during P2L1 for surface Chla. This increase agrees with that estimated from weekly SeaWiFS products, although surface Chla appears to peak too early in the model, by about 1–2 weeks.

[30] NP and RP were sampled at fewer stations than nitrate and Chla during P2L1. On average, the increase of NP in the model from 3 to  $5 \text{ mmolN m}^{-2} \text{ d}^{-1}$  between P1L2 and P2L1, is consistent with the data. RP values in the model are also in the same range than the observations. In terms of the  $f$ -ratio, the same increase from 0.4 to 0.6 is estimated from the model as from the in situ measurements.

[31] The agreement with the P2L2 data is less satisfactory. The model does predict a secondary bloom during P2L2, in response to the deepening of the ML, but the amplitude of this bloom is highly underestimated. We will come back on the issue in the discussion.

[32] A significant increase in zooplankton between P1 and P2 is predicted by the model, in agreement with the increase observed between P1L2 and P2L2. However, zooplankton concentrations in the model seem to be overestimated. This could be due to many factors such as the large uncertainties in the conversion to nitrogen, the contribution of mixotroph dinoflagellates to grazing (which is not accounted for in the data) or an oversimplification in the representation of zooplankton in the model.

## 4.2. Large-Scale Bloom Propagation: Time Versus Latitude Variability

[33] Figure 7 provides a more complete view of the system evolution between P1 and P2, showing the time evolution of model outputs averaged in the zonal direction. The MLD retreat is earlier by about 2 weeks in the south compared to the north. This causes an earlier bloom onset in the south. This bloom propagation results in two different situations: one at the beginning of March (during P1L2), with more phytoplankton and NP in the south than in the north, and the opposite situation during P2 and afterward. Comparison of NP with MLD and nitrate reveals that light (MLD) controls the NP evolution in March, while nutrient availability controls the meridional propagation of NP afterward. On the whole, the initial meridional large-scale gradient in nitrate induces a phytoplankton meridional gradient during P2, and a zooplankton meridional gradient by the end of the 3 month experiment.

[34] Another noticeable aspect of this particular bloom is its long duration. North of  $41^\circ\text{N}$ , the bloom lasts 2 months, with a 1 month onset, and 1 month decay. In March, nutrient levels remain practically unchanged, despite consumption by photosynthesis. There is a strong coupling between PP and grazing during P2.

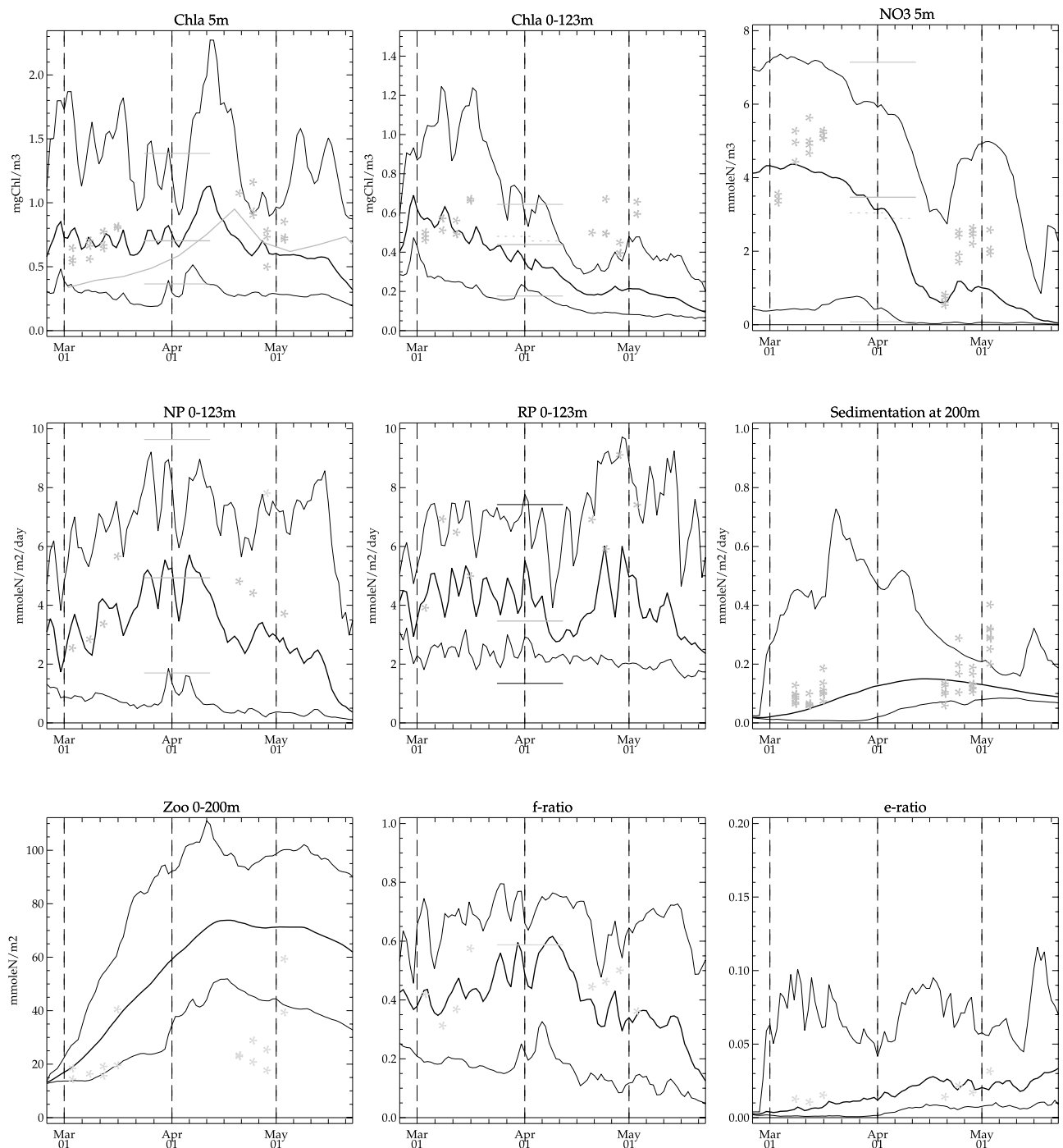


**Figure 6.** Comparison of the biological model results with data. For each field the bold line shows the time evolution of the result from the model, averaged over the model domain. The thin lines show the model minimum and maximum values. Data are shown in shading. Shaded asterisks show the data of the L2 time series stations. Shaded bars show the data of P2L1 (the length of the bar corresponds to the duration of the leg), averaged over the domain (bold line) and its bounds (thin lines). The shaded dashed lines (on the Chla 0–123 m and NO3 5 m plots) show the data of P2L1, averaged during the first part of the leg (16.5–18.5W, 38.5–43N) and the second part of the leg (18.5°–21°W, 38.5°–43°N) (see Figure 1). The shaded line on the surface Chla plot is the average over the POMME domain of weekly level 3 Sea-viewing Wide Field-of-view Sensor (SeaWiFS) composites.

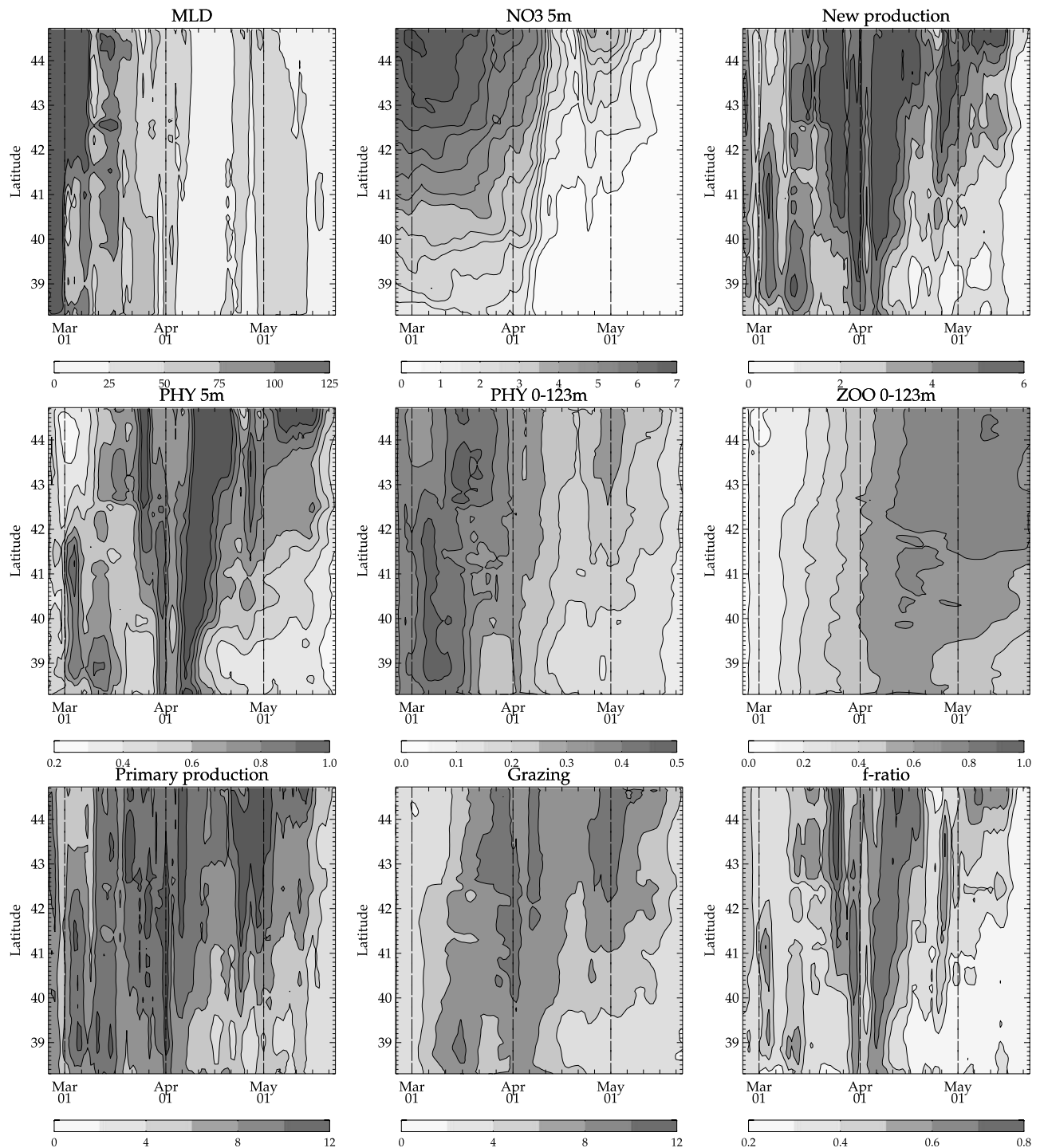


**Figure 7.** Time evolution of model outputs averaged in the zonal direction of the MLD (in meters, contours 25 m), the nitrate concentration at the surface ( $\text{NO}_3$  5 m, contour  $0.5 \text{ mmolN m}^{-3}$ ), new production (contour  $1 \text{ mmolN m}^{-2} \text{ d}^{-1}$ ), phytoplankton concentration at the surface (PHY 5 m, contour  $0.1 \text{ mmolN m}^{-3}$ ), phytoplankton concentration averaged in the top 123 m (PHY 0–123 m, contour  $0.05 \text{ mmolN m}^{-3}$ ), zooplankton concentration averaged in top 123 m (ZOO 0–123 m, contour  $0.1 \text{ mmolN m}^{-3}$ ), primary production (contour  $2 \text{ mmolN m}^{-2} \text{ d}^{-1}$ ), phytoplankton grazing by zooplankton (contour  $2 \text{ mmolN m}^{-2} \text{ d}^{-1}$ ), and  $f$ -ratio (contour 0.2).

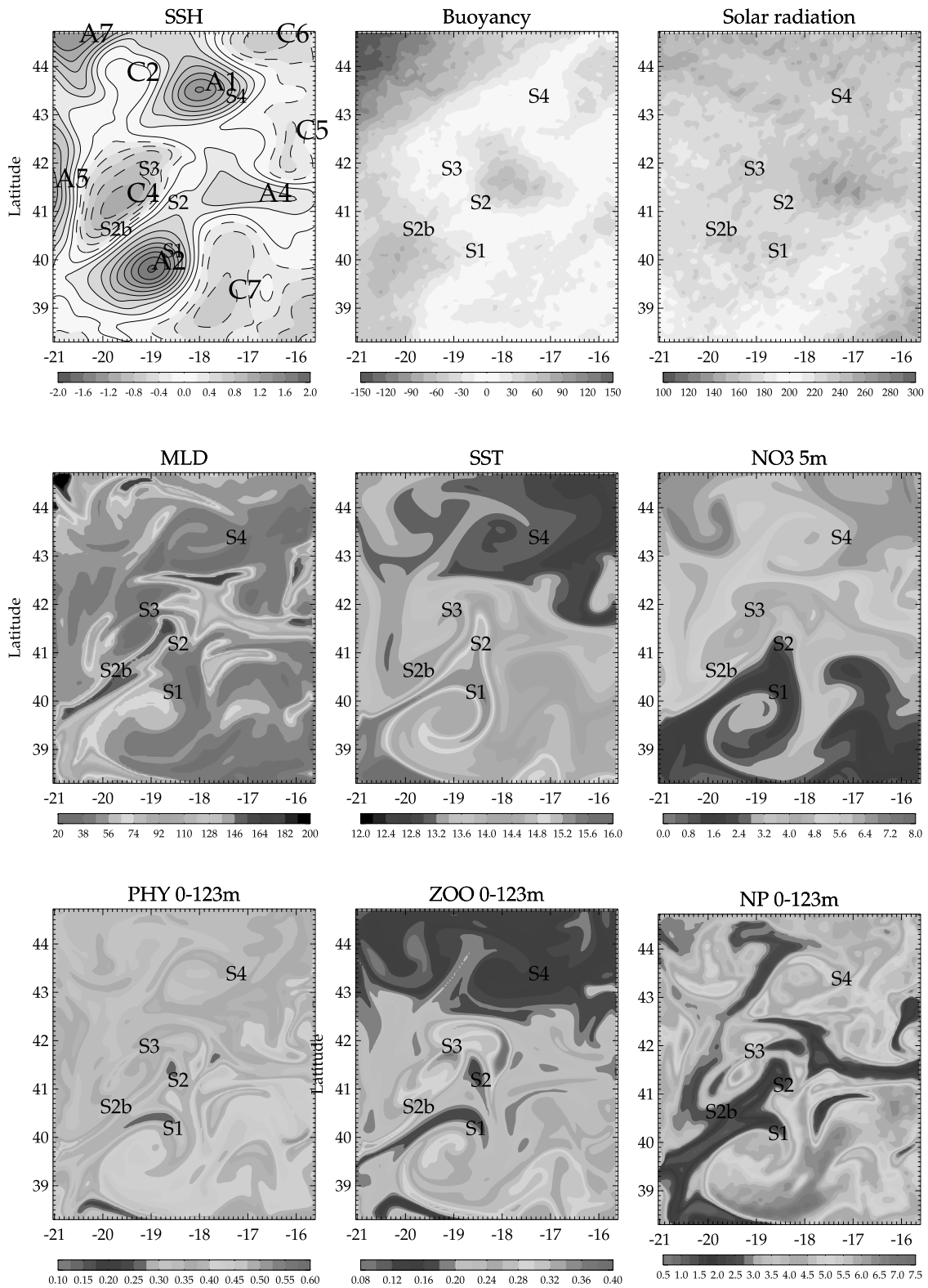


**Figure 8.** Snapshots of model outputs during P1L2 (11 March 2001). Also indicated are the locations of the time series stations. See color version of this figure at back of this issue.

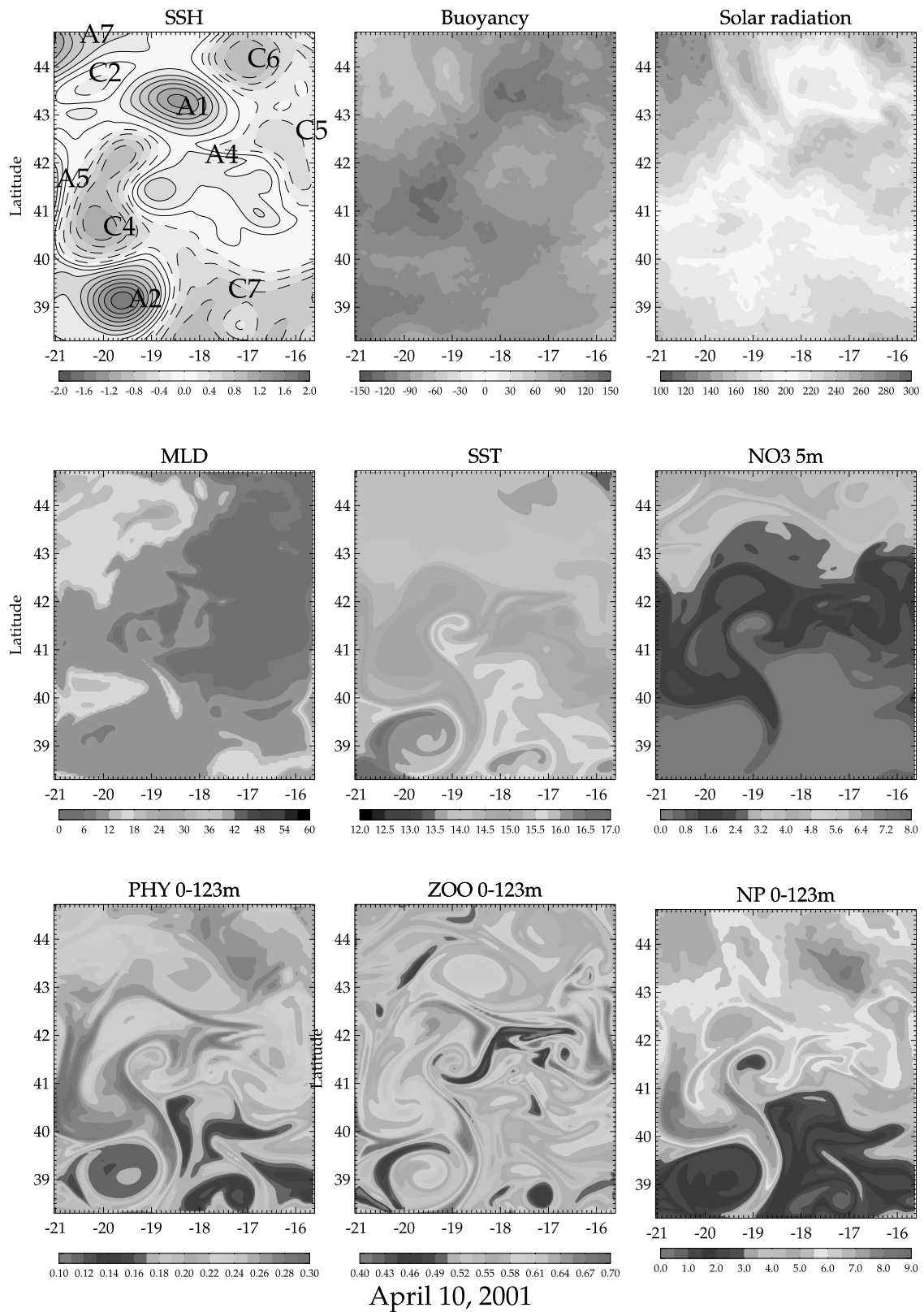


**Figure 9.** Snapshots of model outputs during P2L1 (10 April 2001). Note that the color scales are not always the same as in Figure 8. See color version of this figure at back of this issue.

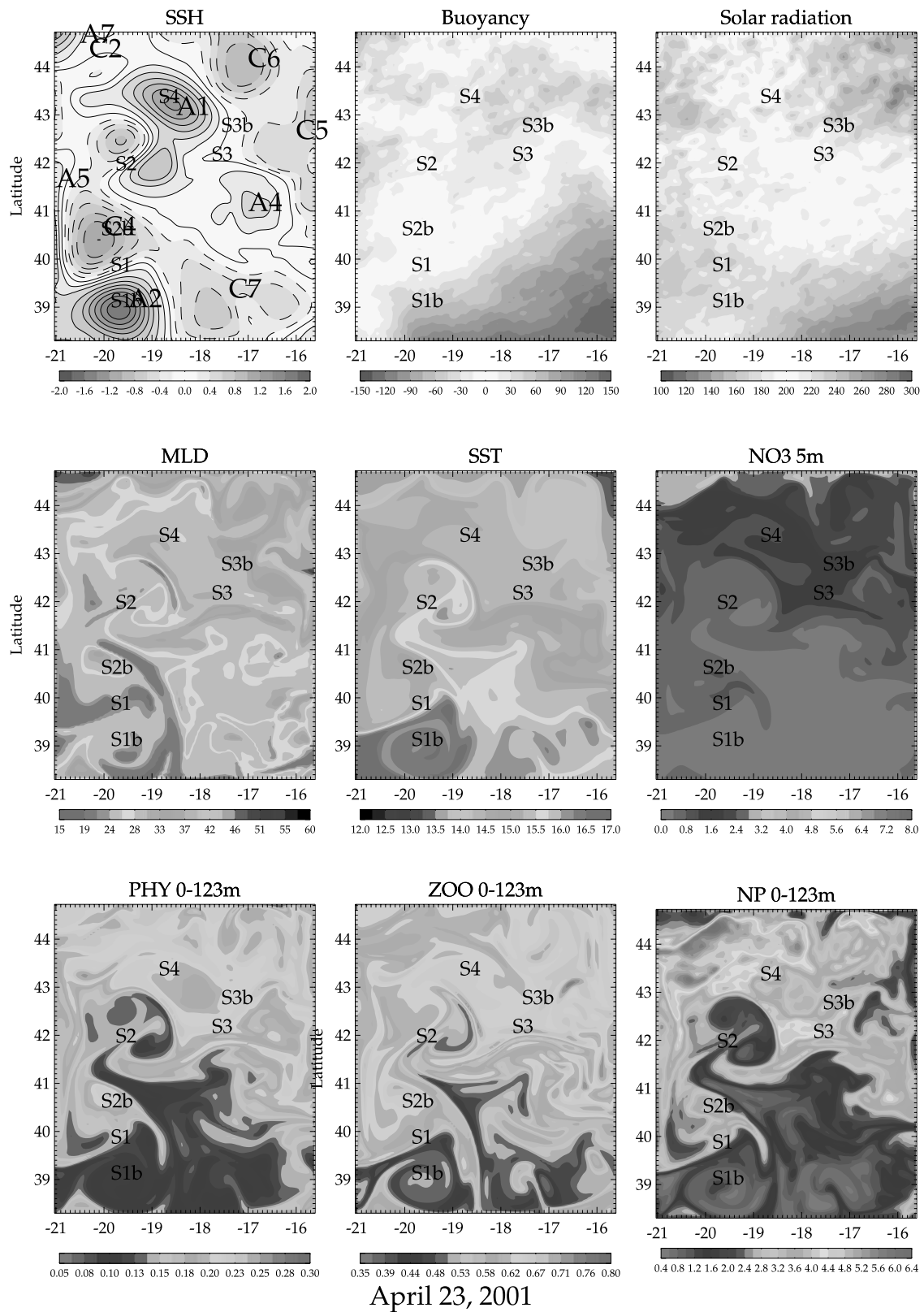


**Figure 10.** Snapshots of model outputs during P2L2 (23 April 2001). Note that the color scales are not always the same as in Figures 8 and 9. Also indicated are the location of the time series stations. See color version of this figure at back of this issue.

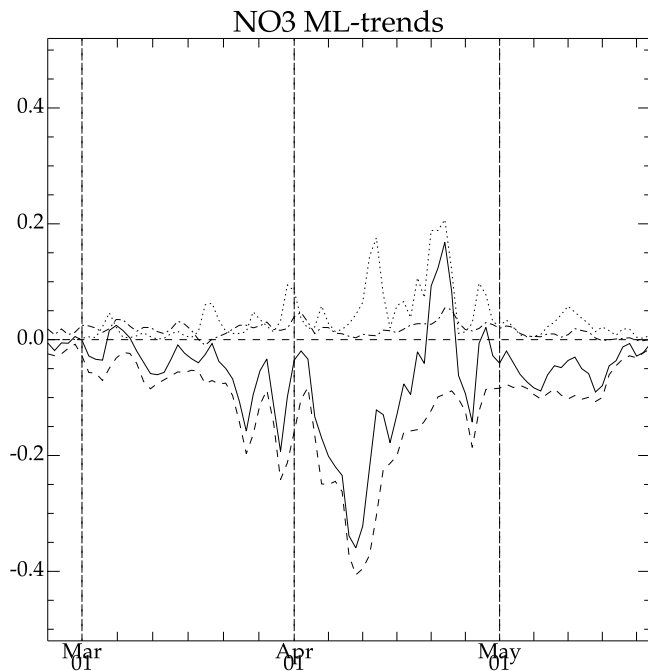


**Figure 11.** Time evolution of the trends in the nitrate equation in the mixed layer averaged over the model domain (in  $\text{mmolN m}^{-3} \text{d}^{-1}$ ). The solid line shows  $\overline{(\partial\text{NO}_3/\partial t)} = \overline{(\partial\text{NO}_3/\partial t)} + \text{ent}$ , the dotted line shows vertical diffusion  $\overline{(\partial/\partial z)(k_z(\partial\text{NO}_3/\partial z))}$ , the dashed line shows biological consumption minus nitrification  $\overline{S(\text{NO}_3)}$ , and the dash-dotted line shows total advection  $-\overline{\nabla(\mathbf{u}\text{NO}_3)}$ . The varying mixed layer depth is  $h$ . Overbars denote the mixed layer average:  $\bar{a} = (1/h)\int_{-h}^0 adz$ . The entrainment of water from below  $\text{ent} = (1/h)((\partial h/\partial t)(\text{NO}_3(-h) - \overline{\text{NO}_3}))$  (not shown) can only be computed as the residual of the other terms with the discretized form of the equations used in OPA [Vialard and Delecluse, 1998] and is generally small in comparison with the vertical diffusion flux (J. Vialard and G. Madec, personal communication, 2004).

[35] In the simulation, MLD deepening events permit nutrient reloading, thus prolongating the bloom (for instance on 1 April), or initiating secondary postblooms (as during P2L2, at the end of April). The P2L2 reload is particularly obvious in the northern part of the domain between 22 and 27 April, and is followed by a significant increase in the total phytoplankton stock.

### 4.3. Mesoscale and Submesoscale Variability

#### 4.3.1. Bloom Onset (P1L2)

[36] Space variability during P1L2 is illustrated by Figure 8, which shows a snapshot of model outputs on 11 March. Compared with the initial state (Figure 2), the main evolution in the eddy field occurs at the boundary between A2 and C4, which has rotated toward the northeast. Associated with this meandering, there is an intrusion of cold and nutrient-rich waters along the western model boundary, and a northward advection of warm waters along  $18.5^\circ\text{W}$ .

[37] A very striking feature is the strong variability of the MLD on filamentary scales. The small-scale features in

MLD are particularly intense during the period of stratification [Paci et al., 2005; Giordani et al., 2005]. The maximum MLD gradient is reached at the border of A1, where MLD changes from 200 m to 50 m over 10 km. These fine-scale structures in the MLD seem to result from the interplay between the mesoscale atmospheric forcing and the stirring induced by the eddies. The medium-scale picture is that MLD is shallower over the regions previously subjected to warming (in the southeast and northeast) and that it is deeper over the regions subjected to cooling (in the northwest, in the center, and in the southwest). This medium-scale picture is perturbed by the small-scale advection, which induces a direct cascade of the MLD toward smaller scales. Areas of minimum MLD include the borders of A1, A2, A5 and C7, while the MLD is particularly deep in the fronts between A2 and C4, A1 and C4, and around C2.

[38] At medium scale, NP and phytoplankton variability is driven by the variability of the buoyancy flux and of the solar radiation. At small scale, NP and phytoplankton patterns follow the MLD distribution. NP is maximum over the filamentary structures of MLD minima, and conversely NP is minimum over the filaments of maximum MLD. The mesoscale dynamics therefore contribute to structuring the initial conditions for the onset of the spring bloom in specific submesoscale features. There is no nutrient limitation yet. The structuring is mainly the consequence of photosynthesis limitation by (lack of) light, which is greater when the MLD is deeper.

#### 4.3.2. Bloom Decay (P2L1)

[39] The situation on 10 April (Figure 9) is quite different. C4 and A2 have continued to interact. The front between the southern and northern waters is very well defined in SST, as well as in other properties such as nitrate and phytoplankton. Exchanges take place at the front, around eddies. Particularly remarkable is the intrusion of northern waters along the western flank of C4 and eastern flank of A2, down to the southern boundary of the model. One can also see the formation of a small anticyclone of southern waters detaching from the front.

[40] Buoyancy forcing is positive everywhere, and the MLD shows little variability. Nutrients are exhausted south of the meandering front. NP is structured by the large-scale nutrient gradient and the water exchanges at the front. Another factor influencing NP is solar radiation. In the north, there is a factor two change in NP between the east and the west, that mirrors a similar change in solar radiation. The small-scale structures in NP and phytoplankton are

**Table 3.** Simulated Production and Export Budgets Between 22 February and 31 May 2001<sup>a</sup>

	Total	South	North
PN	255	199	297
RP	319	301	332
PP	574	500	629
EP	27	25	28
<i>f</i> -ratio	0.44	0.40	0.47
<i>e</i> -ratio	0.05	0.05	0.04

<sup>a</sup>Total is average over the inside domain. North and south are averages north and south of  $41^\circ\text{N}$ , respectively. Units are  $\text{mgC m}^{-2} \text{d}^{-1}$ . Nitrogen rates have been converted to carbon using a standard Redfield ratio, ignoring the large seasonal changes in the PP C:N ratio that have been reported [Kortzinger et al., 2001].

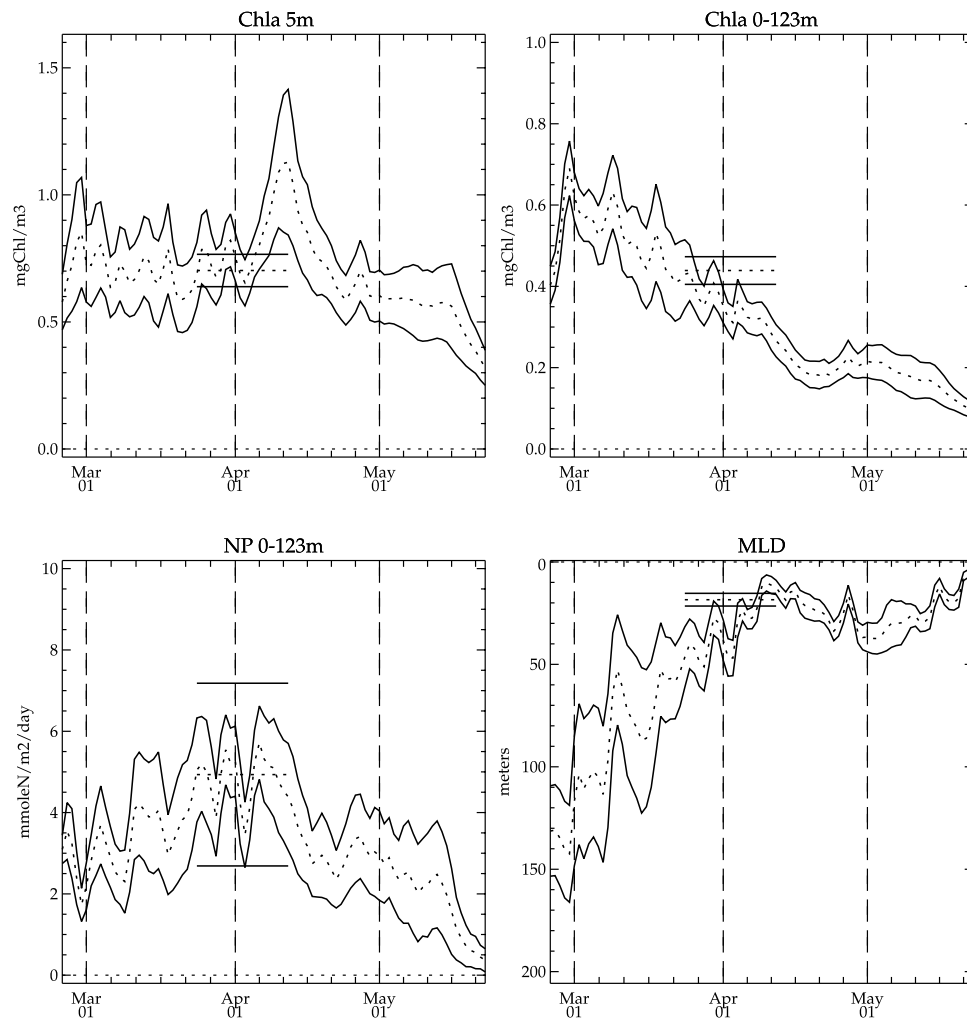


**Figure 12.** Model mean (dotted line)  $\pm$  standard deviation (solid lines) for surface Chla, integrated Chla, new production, and mixed layer depth. Horizontal lines show mean and standard deviation computed from the P2L1 arrays.

associated with the across front filamentary exchanges of nitrate. The filament that extends south around A2 causes local PP changes of a factor 2.5 over 10 km. Besides this filament and the small eddy, the small-scale structures in the phytoplankton field are much less energetic. This is not the case for zooplankton, which show more energetic variability at the mesoscale and submesoscale. Zooplankton are more abundant inside A1, which embodies waters where the bloom has started earlier due to earlier stratification (Figure 8).

#### 4.3.3. Secondary Bloom (P2L2)

[41] The atmospheric depression that passes through the north of the POMME area during P2L2 is responsible for the destratification of the water column and the deepening of the MLD. This deepening is most pronounced in the northeast corner, above C5 and C6, with MLDs reaching 50 m by 23 April (Figure 10). Nitrate was depleted previous to the storm, and is reinjected at the surface through the erosion of the ML. This enables a secondary bloom in the north. Again, the structure of this bloom is modulated at small scales by the MLD and at larger scale by variations in the solar radiation. A particular feature of

interest is the mushroom-like intrusion of nutrient-poor southern waters south of A1. One of such features has been tele-detected by SeaWiFS during POMME (H. Loisel and Y. Lehahn, personal communication, 2004).

## 5. Discussion

### 5.1. Specificities of the Spring Bloom During POMME

#### 5.1.1. Bloom Intensity and Duration

[42] This modeling study has enabled the identification of unexpected characteristics of the spring bloom for the region. The increase and subsequent decrease of primary production (PP) occurs over a relatively long period of time, which extends from March to May. Although long in duration, the maximum chlorophyll values are small ( $1.1 \text{ mgChl m}^{-3}$  on average) compared to values of the order of 2 to  $3 \text{ mgChl m}^{-3}$  previously reported between  $40^\circ\text{N}$  and  $47^\circ\text{N}$  in the north Atlantic [Lochte *et al.*, 1993; Sieracki *et al.*, 1993; Harrison *et al.*, 1993; Bury *et al.*, 2001].

[43] During the onset of the bloom, the decline of nitrate is rather slow. In the ML, biological consumption

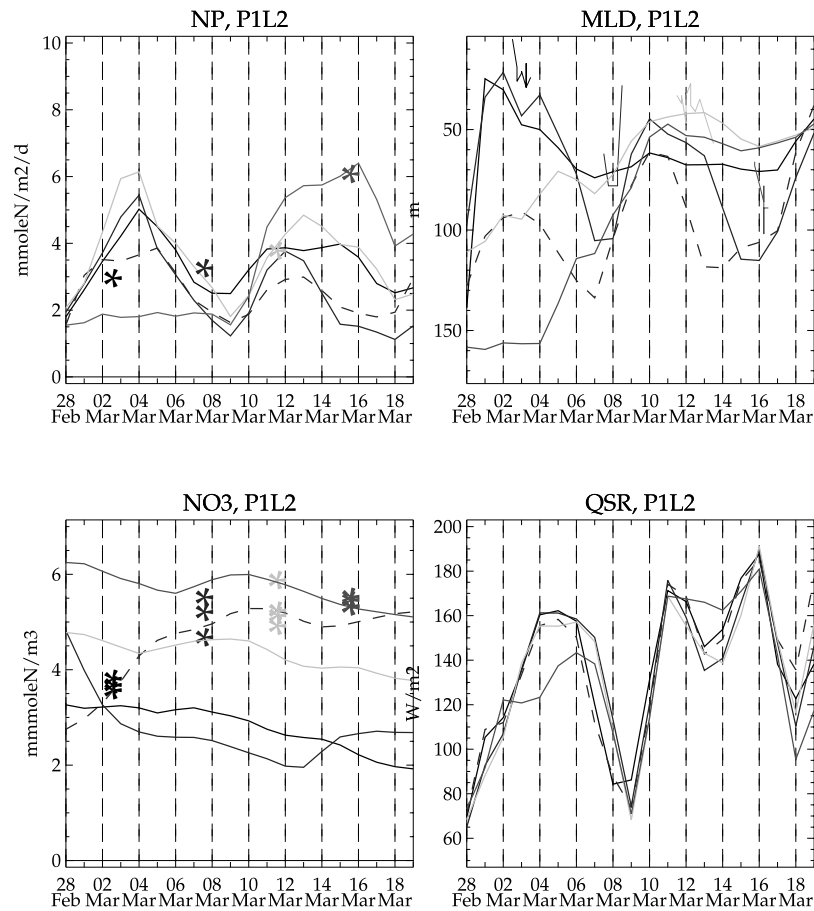


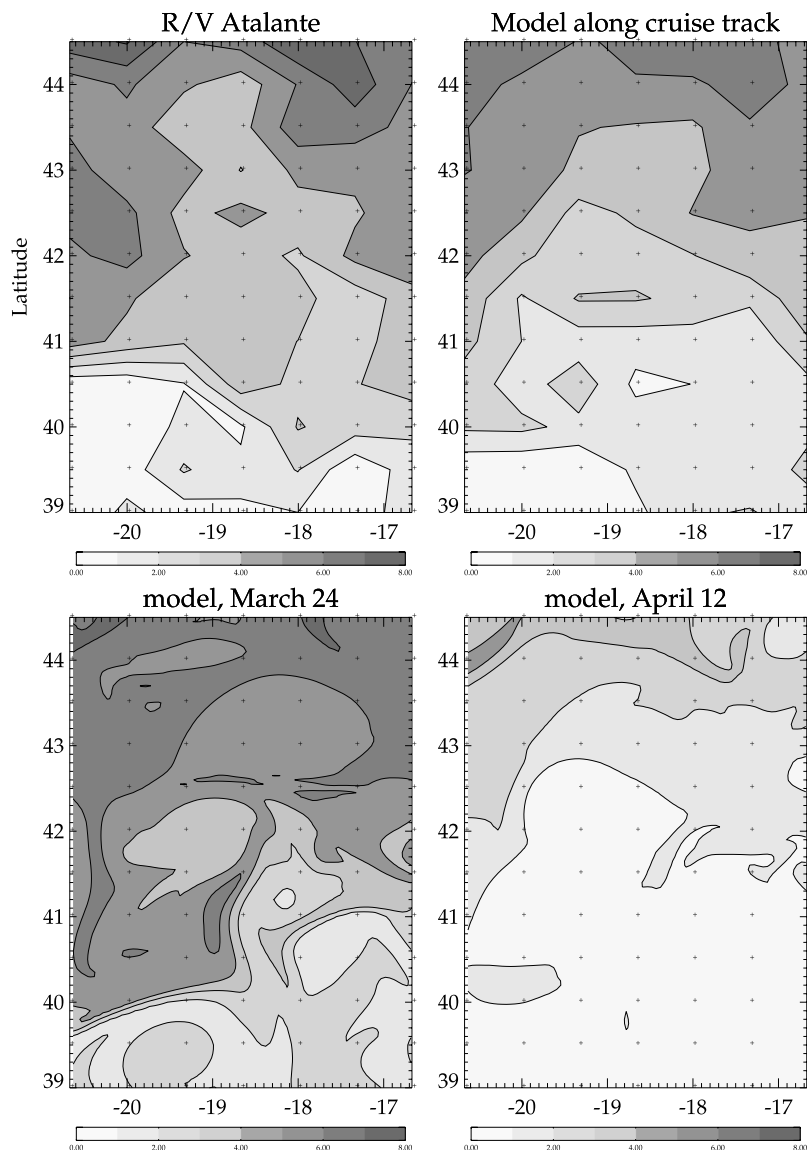
**Figure 13.** Time evolution during P1L2 of the model new production (NP), mixed layer depth (MLD), surface nitrate concentration (NO<sub>3</sub>), and solar radiation (QSR) at stations S1 (black), S2 (blue), S2b (dashed blue), S3 (green), and S4 (red), compared with the observations (asterisks for surface nitrate and NP, thin lines for MLD time series). See color version of this figure at back of this issue.

is partly compensated by a series of vertical diffusion events (Figure 11). The slow bloom onset is attributable to the succession of atmospheric depressions in March, the delay in stratification and intermittent nutrient reloading of the surface layer. Examination of SeaWiFS data [Lévy *et al.*, 2005] actually suggests that the bloom has started prior to P1 north of 41°N. The midlatitude regime that they identify is intermediate between the subpolar and subtropical regimes: the bloom starts as an entrainment bloom (i.e., with the deepening of the ML, as in the subtropics) and ends as a subpolar bloom (i.e., it reaches its maximum after the retreat of the ML). In April, the weather becomes milder and nitrate consumption is less efficiently compensated by dynamical supplies.

[44] The long bloom duration and the rather weak surface phytoplankton concentration could only be obtained in the model with a strong coupling between phytoplankton and zooplankton. Figure 7 shows that, integrated over the upper 123 m, grazing slightly exceeds PP during P2, which explains the decline in integrated phytoplankton. This is not the case in the ML where PP is maximum and exceeds grazing, and phytoplankton concentration increases. Over a hundred sensitivity analyses on the model parameters were conducted during the course of this study. They emphasized the control by zooplankton of the rate of nitrate decrease

and phytoplankton stock. Given the phytoplankton taxonomy that highlights the dominance of small phytoplankton species [Claustre *et al.*, 2005], this coupling very likely involves microzooplanktonic organisms. The phytoplankton growth rate in the model ( $1.04 \text{ d}^{-1}$ ) is in the low range of commonly accepted values in the literature ( $1\text{--}2 \text{ d}^{-1}$ ), thus implicitly taking into account colimitations (by silicate, iron) that are suggested by incubation experiments [Blain *et al.*, 2004; Leblanc *et al.*, 2005]. The zooplankton growth rate ( $0.8 \text{ d}^{-1}$ ) is close to that of phytoplankton. The strong coupling between phytoplankton and zooplankton is consistent with the modeling study of Popova *et al.* [2002], conducted in the northeast Atlantic to reproduce the variability during the 1997 Discovery cruise 227, and suggesting a strong influence of zooplankton in the region.

[45] In contrast with results from other mesoscale numerical models [McGillicuddy *et al.*, 1995b; Lévy *et al.*, 2000] the bloom duration is not extended by advective nutrient inputs associated with mesoscale eddies. Figure 11 shows that advection is a small contribution to the ML nutrient budget, even during the postbloom period. Vertical velocities at 100 m in the model are less than  $5 \text{ m d}^{-1}$ , which is at the low end of the range of estimates from earlier field studies for mesoscale flows ( $40 \text{ m d}^{-1}$  estimated by Pollard and Regier [1992]). Estimates of vertical velocities in



NO<sub>3</sub>, POMME 1 LEG2

**Figure 14.** Nitrate at the surface during P2L1. (top) Data gathered along the track of the R/V *l'Atalante* and model results along the track (dots show the approximate location of the CTD stations). (bottom) Model results at the beginning and the end of the leg.

POMME from drifters is still in progress and should provide some new insights. The small  $w$  values in the model are consistent with the apparent steadiness of the geostrophic horizontal currents during the surveys, and the low eddy kinetic energy. A sensitivity experiment was conducted with assimilation of altimetric sea level anomaly in order to better constrain the eddies. In this simulation, NP level remained unchanged. This apparently contrasts with the result of *Oschlies and Garçon* [1998], where the NP budget at the same latitudes was greatly increased by assimilation. Indeed, with the resolution used in this study (1/20 of a degree compared with 1/3 of a degree in the work of *Oschlies and Garçon* [1998]), assimilation of altimetry does not boost the mesoscale dynamics, which are already well represented by the model.

### 5.1.2. Production and Export Budgets

[46] Table 3 shows the simulated production and export budgets during the 3 months of the experiment. PP during POMME is in lower range of what has been previously reported [*Bury et al.*, 2001]. Maybe the most unexpected result of POMME is that RP accounts for more than half PP during the bloom, and the average  $f$ -ratio is lower than 0.5. Since nitrification is not taken into account in our definition of the  $f$ -ratio, this value should be considered as an upper bound. Large regenerated production and relatively low  $f$ -ratios have already been reported in the northeast Atlantic (see *Bury et al.* [2001] for a review), but in the range 0.6 (during NABE [*Garside and Garside*, 1993]) to 0.7 [*Bury et al.*, 2001]. The large regenerated production could only be correctly simulated in the model with a large initial

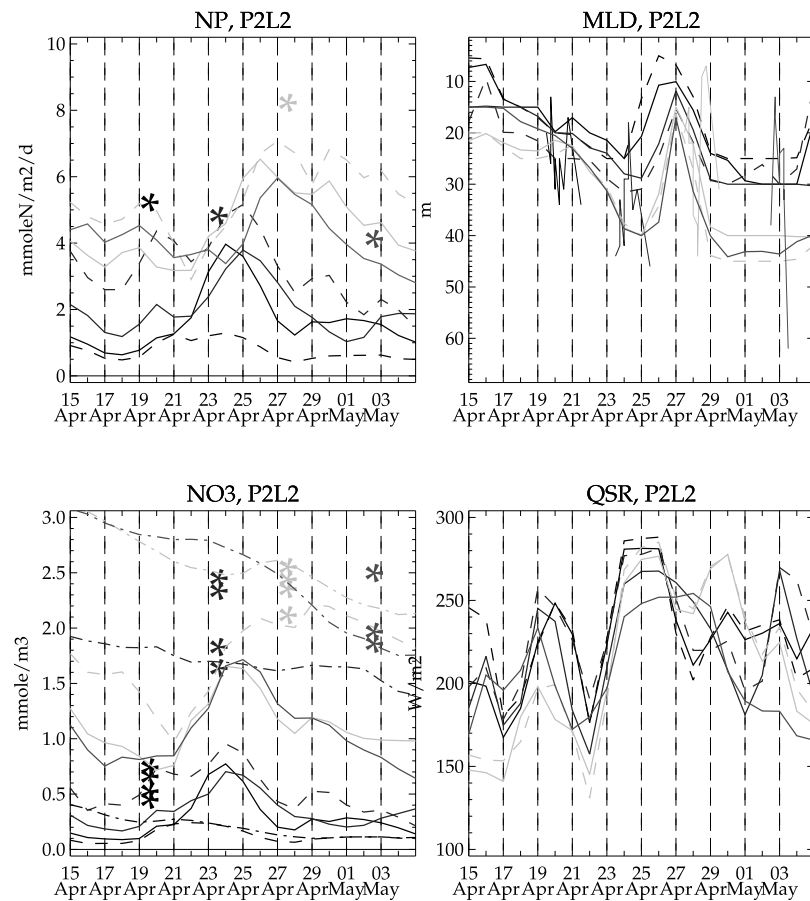


**Figure 15.** Time evolution during P2L2 of the model new production, mixed layer depth, surface nitrate concentration, and solar radiation at stations S1 (black), S1b (dashed black), S2 (blue), S2b (dashed blue), S3 (green), S3b (dashed green), and S4 (red) compared with the observations (asterisks for surface nitrate and NP, thin lines for MLD time series). Nitrate concentration at the observed mixed layer depth and at stations S1, S2b, S3b, and S4 are shown with dash-dotted lines. See color version of this figure at back of this issue.

source of semilabile DON, which is progressively remineralized to ammonium (Table 2). Although total organic nitrogen data seem to agree with this high initial value, work is still in progress to examine the seasonal variability of the semilabile DON stock (P. Raimbault, personal communication, 2004). The question of the origin of the large regeneration remains [Fernandez *et al.*, 2005a]. In the real ocean, large DON concentrations could result from Ekman transport from the north as suggested by Williams and Follows [2003]. Alternatively, a very rapid and efficient regeneration process may be missing in the model.

[47] The  $e$ -ratio is small during this bloom period (5%), both in the model and in the observations. In the model, this has been achieved by taking into account only slow ( $3 \text{ m d}^{-1}$ ) sinking particles. This suggests that a large contribution of the export is achieved later in the season, either in the form of sinking particles (but this hypothesis seems not to be confirmed by the results of fixed sediment traps [Guieu *et al.*, 2005]) or rather through winter convection of dissolved organic material. This is the case at similar latitudes in the Mediterranean Sea [Lévy *et al.*, 1998]. Estimates of the  $e$ -ratio at  $47^\circ\text{N}$  during NABE [Bender *et al.*, 1992] are slightly higher (13%), but consistent with the POMME estimate in view

of the rapid change of regime at these latitudes [Lévy *et al.*, 2005].

## 5.2. Space Versus Time Variability

### 5.2.1. Small-Scale Variability

[48] Results of this study have revealed strong variability of the spring bloom on short time- and space scales. As seen before, variability on short timescale is mainly due to the synoptic variability in the atmosphere, variability at mesoscale to the mesoscale variability in the atmosphere, and variability at submesoscale to the stirring induced by mesoscale eddies. The relative importance of time and space variabilities are compared in Figure 12, which shows the time evolution of the model mean and standard variations, for MLD, NP and Chla. In order to remove the contribution of the north-south gradient, the zonal average is subtracted before the computation of the standard deviation. Therefore standard deviation quantifies the variability associated with the mesoscale and submesoscale. The standard deviation estimated from the P2L1 arrays is also represented. The vertical distance between the two plain lines is twice the standard deviation, which is a measure of the average variation on small scales. The standard deviation in the model is of the same order of that estimated from the P2L1

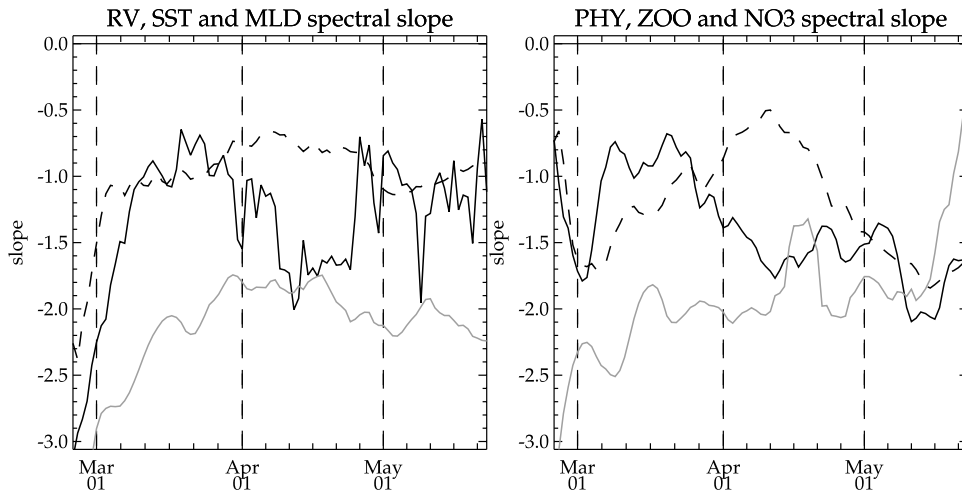


**Figure 16.** Time evolution of the slope of the two-dimensional Fourier autospectra of (left) MLD (solid line), surface relative vorticity (dashed line), and SST (shaded line) and (right) integrated phytoplankton (solid line), integrated zooplankton (dashed line), and surface nitrate (shaded line).

array. Figure 12 shows that on short timescales (2–3 days), time and space variability are of the same order of magnitude. However, on seasonal timescale, seasonal variability is the dominant trend. This result suggests that it is reasonable to derive seasonal budgets from P1L1 and P2L1 arrays, but that the separation between time and space variability in the interpretation of P1L2 and P2L2 data, and the interpretation of spatial structures in P1L1 and P2L1 arrays, are extremely difficult tasks.

**5.2.2. Asynopticity During P1L2**

[49] Figure 13 shows the time evolution during P1L2 of NP, MLD, nitrate and solar radiation at the four time series stations (Figure 8), compared with the observations. S1 is located inside A2, S2 is at the front between A2 and C4, S3 is located inside C4 and S4 inside A1. We also show the results of an additional station S2b, also located at the front.

[50] The agreement between the model prediction and the observations is generally very good. One exception is the

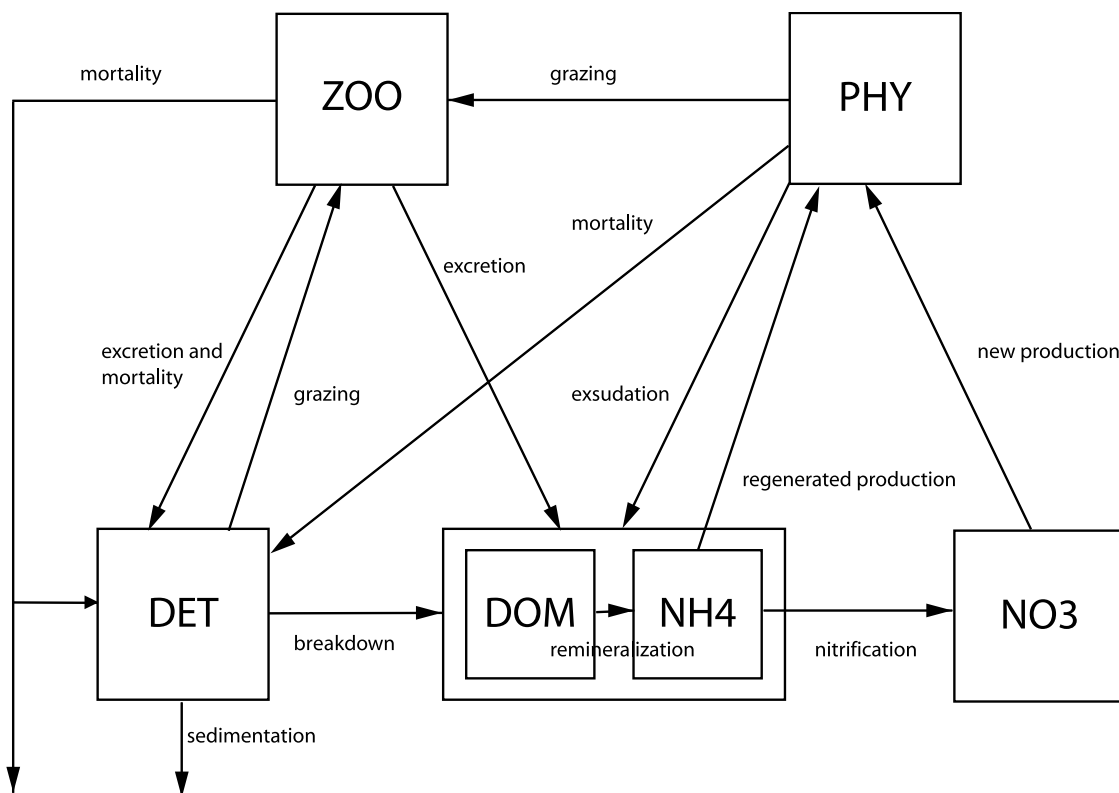


**Figure A1.** Diagram of the Lodyc Ocean Biogeochemical Simulation Tools for Ecosystem and Resources (LOBSTER) biological model.

**Table A1.** Biological Equations in the Euphotic Layer

Description	Equation
Tracer transport	$\frac{\partial C}{\partial t} = S(C) - \nabla(\mathbf{u}C) + \frac{\partial}{\partial z}(k_z \frac{\partial C}{\partial z}) + D_{\text{lat}}$ (1)
Nitrate source/sink	$S(\text{NO}_3) = -\mu_p L_I L_{\text{NO}_3} P + \mu_n \text{NH}_4$ (2)
Ammonium source/sink	$S(\text{NH}_4) = f_n \gamma \mu_p L_I (L_{\text{NO}_3} + L_{\text{NH}_4}) P - \mu_p L_I L_{\text{NH}_4} P - \mu_n \text{NH}_4 + f_n (\mu_z Z + \mu_d D + \mu_{\text{dom}} \text{DOM})$ (3)
Phytoplankton source/sink	$S(P) = (1 - \gamma) \mu_p L_I (L_{\text{NO}_3} + L_{\text{NH}_4}) P - G_p - m_p P$ (4)
Zooplankton source/sink	$S(Z) = a_z (G_p + G_d) - m_z Z^2 - \mu_z Z$ (5)
Detritus source/sink	$S(D) = (1 - a_z) (G_p + G_d) + m_p P - G_d + f_z m_z Z^2 - \mu_d D - V_d \partial_z D$ (6)
DOM source/sink	$S(\text{DOM}) = (1 - f_n) (\gamma \mu_p L_I (L_{\text{NO}_3} + L_{\text{NH}_4}) P + \mu_z Z + \mu_d D) - \mu_{\text{dom}} \text{DOM}$ (7)
Chlorophyll	$\text{Chl} = R_{\text{Chl:N}} P$ (8)
Chlorophyll:nitrogen ratio	$R_{\text{Chl:N}} = \max(R_{\text{Chl:N}}^{\min}, R_{\text{Chl:N}}^{\max} - (R_{\text{Chl:N}}^{\max} - R_{\text{Chl:N}}^{\min}) \frac{\overline{\text{PAR}}}{\text{PAR}_{\max}})$ (8)
Light limitation	$L_I = 1 - e^{-\frac{\text{PAR}}{K_{\text{par}} \frac{R_{\text{Chl:N}}}{R_{\text{Chl:N}}^{\text{ref}}}}}$ (9)
Nitrate limitation	$L_{\text{NO}_3} = \frac{\text{NO}_3}{\text{NO}_3 + K_{\text{no}_3}} e^{-\psi \text{NH}_4}$ (10)
Ammonium limitation	$L_{\text{NH}_4} = \frac{\text{NH}_4}{\text{NH}_4 + K_{\text{nh}_4}}$ (11)
Grazing of phytoplankton	$G_p = g_z \frac{pP}{K_z + pP + (1-p)D} Z$ (12)
Grazing of detritus	$G_d = g_z \frac{(1-p)D}{K_z + pP + (1-p)D} Z$ (13)
Preference for phytoplankton	$p = \frac{\tilde{p}P}{(\tilde{p}P + (1-\tilde{p})D)}$ (14)

nitrate concentration which is underestimated by the model at S2, but in much better agreement at S2b. Figure 8 reveals that this frontal region coincides with a strong nitrate front, which explains that different nitrate concentrations are found at these neighboring stations.

[51] Nitrate is not the limiting factor for NP during this period. The model reveals that at stations S1, S2, S2b and S3, NP variations are very similar. NP varies by a factor 3 over periods of 2 to 3 days. Figure 13 clearly reveals that these variations are the consequence of strong changes in the solar radiation. The situation is different at station S4, which is located further north. The MLD retreat occurs a week later, causing a delayed increase in NP. NP is also higher at this station. In the model, this is due to the grazing pressure that is not yet as efficient in the north as in the south (Figure 7).

[52] On the whole, these results suggest that the observation of similar NP at stations S1, S2 and S3 is mainly accidental. There seem to be more variability than the data suggest, and this variability is primarily driven by large day to day changes in the solar radiation. Moreover, the time variability revealed by the model is stronger than the variability associated with the location in the eddy field (i.e., between the stations). This last remark should be regarded critically, since variability in winter preconditioning (of phytoplankton and zooplankton) at the mesoscale is omitted in the model. *Popova et al. [2002]* have identified a contrasting situation, where they attribute mesoscale variability mostly to variability in zooplankton preconditioning.

### 5.2.3. Asynopticity During P2L1

[53] Figure 14 shows 4 different snapshots of nitrate at the surface during P2L1. The first map shows the data

**Table A2.** Biological Parameters

Parameter Name	Symbol	Value	Unit
Nitrate limitation half-saturation value	$K_{\text{no}_3}$	0.7	$\text{mmol m}^{-3}$
Ammonium limitation half-saturation value	$K_{\text{nh}_4}$	0.001	$\text{mmol m}^{-3}$
Inhibition of nitrate uptake by ammonium	$\psi$	3	
Light limitation half-saturation value	$K_{\text{par}}$	33.0	$\text{W m}^{-2}$
Phytoplankton maximal growth rate	$\mu_p$	$1.21 \times 10^{-5}$	$\text{s}^{-1}$
Phytoplankton exudation rate	$\gamma$	0.05	
Phytoplankton mortality rate	$m_p$	$5.80 \times 10^{-7}$	$\text{s}^{-1}$
Grazing half-saturation value	$K_z$	1.0	$\text{mmol m}^{-3}$
Zooplankton maximal grazing rate	$g_z$	$9.26 \times 10^{-6}$	$\text{s}^{-1}$
Assimilated food fraction by zooplankton	$a_z$	0.7	
Preference for phytoplankton	$\tilde{p}$	0.5	
Zooplankton excretion rate	$\mu_z$	$5.80 \times 10^{-7}$	$\text{s}^{-1}$
Zooplankton mortality rate	$m_z$	$2.31 \times 10^{-6}$	$\text{s}^{-1} \text{mmol}^{-1} \text{m}^3$
Fraction of slow sinking mortality	$f_z$	1.0	
Nitrification rate	$\mu_n$	$5.80 \times 10^{-7}$	$\text{s}^{-1}$
DOM breakdown rate	$\mu_{\text{dom}}$	$3.86 \times 10^{-7}$	$\text{s}^{-1}$
Ammonium/DOM redistribution ratio	$f_n$	0.75	
Detritus sedimentation speed	$V_d$	$3.47 \times 10^{-5}$	$\text{m s}^{-1}$
Detritus remineralization rate	$\mu_d$	$5.78 \times 10^{-7}$	$\text{s}^{-1}$
Minimum Chl:N ratio	$R_{\text{Chl:N}}^{\min}$	1.0	$\text{mgChl/mmolN}$
Maximum Chl:N ratio	$R_{\text{Chl:N}}^{\max}$	2.62	$\text{mgChl/mmolN}$
Reference Chl:N ratio	$R_{\text{Chl:N}}^{\text{ref}}$	1.31	$\text{mgChl/mmolN}$
Maximum PAR for Chl:N ratio	$\text{PAR}_{\max}$	5	$\text{W m}^{-2}$

**Table A3.** Optical Model

Description	Equation
Wavelength decomposition	$PAR = PAR_r + PAR_b$ (15)
	$PAR_r(0) = \frac{0.43}{2} Q_{sol}$ (16)
	$PAR_b(0) = \frac{0.43}{2} Q_{sol}$ (17)
Light absorption in red	$PAR_r(z) = PAR_r(z - dz)e^{-k_r dz}$ (18)
Light absorption in blue	$PAR_b(z) = PAR_b(z - dz)e^{-k_b dz}$ (19)
Absorption coefficient in red	$k_r = k_{r0} + \chi_{rp} Pig^{e_r}$ (21)
Absorption coefficient in blue	$k_b = k_{b0} + \chi_{bp} Pig^{e_b}$ (20)
Absorbing pigments	$Pig = \frac{Chl}{r_{pig}}$ (22)

gathered along the track of the R/V *l'Atalante*. The second map is the model result along the same track, with the same space and time resolution. The third and fourth maps are the model results at the beginning and end of the leg, with the model resolution. Comparison between the first two maps shows again a good agreement between the model and data, except for a somewhat stronger depletion of nitrate in the model. This is consistent with the satellite data which shows that the bloom is about a week too early in the model. Most remarkable is the complete change in nitrate distribution predicted by the model between the first and the last day of the leg, from a situation with no nitrate limitation, to a situation with strong limitation south of 42°N. These model results emphasize that the interpretation of maps reconstructed from asynoptic data during P2L1 (such as by *Fernandez et al.* [2005a], *Maixandeau et al.* [2005], and *R. Fukuda-Sohrin and R. Sempéré* (Seasonal distribution in total organic carbon in the northeast Atlantic in 2000–2001, submitted to *Journal of Geophysical Research*, 2004)) must be critically analyzed.

#### 5.2.4. Asynopticity During P2L2

[54] Figure 15 shows the time evolution during P2L2 of NP, MLD, and nitrate at the surface and at the base of the observed ML at the four time series stations (Figure 8), compared with observations. In the observed field (Figure 1), S1 is located inside A2, S2 is inside C4, S4 inside A1, and S3 is located at the front between A1 and A4. In the model (Figure 10), A2 and C4 appear to be located too far south, and the front between A1 and C4 is more diffuse. We therefore added to the analysis stations S1b, S2b and S3b which have locations in the eddy field closer to what should be for S1, S2 and S3.

[55] Generally, NP during P2L2 is underestimated in the model, largely due to the underestimation of the surface nitrate concentration. A close comparison between the modeled and observed MLD suggests an explanation for this underestimation related to underestimation of MLD in situations of strong wind and net warming. In general during this period, the averaged MLD in the model is slightly shallower than the measured MLD. Moreover, the observed MLD reveals large diurnal variability (with amplitudes ranging from 20 m at S1 to 55 m at S4). The underestimation of the MLD in situations of net warming and strong wind (which is the case during P2L2) is a typical shortcoming of vertical turbulent mixing models [*Mellor and Blumberg*, 2004]. It could be due either to the absence of a parameterization (wave breaking, internal waves, etc.) in our 1.5 turbulent closure model and/or to the absence of diurnal cycle forcing. In the nitrate plot of Figure 15 we therefore added the nitrate value at the base of the deepest

observed ML, and compared it with the observed concentrations at the surface. The excellent agreement confirms that the failure of the model in reproducing the intensity of the P2L2 secondary bloom is very likely due to the underestimation of the MLD by the model.

[56] Despite this underestimation, the model enables to give some insight on the observed variability at the four time series stations. The wind event has permitted a reload of nutrients, which do not control NP variability during P2L2. As during P1L2, it is found that variability in NP is largely driven by the variability in solar radiation. In particular, the highest levels of NP observed at S3 are associated with higher solar radiation. At stations S2, S3 and S4, which are located in the northern part of the domain where the wind was most intense, nutrient supplies were higher than at station S1, and the secondary bloom is more intense and lasts longer.

#### 5.3. Spectral Analysis

[57] The model results suggest that the small-scale variability of the MLD and of the nitrate drive a significant small-scale variability of the phytoplankton and zooplankton fields. The emergence of more or fewer energetic small horizontal scales seem to depend on the regime (prebloom, postbloom). In order to quantitatively test that hypothesis and compare the contribution of the various space scales with the total variance of each field, we applied a 2-D fast Fourier transform (FFT) to the variance of the model outputs. We formed auto spectra as a function of a scalar wave number. These spectra exhibit a peak at small wave numbers, and a power law  $k^{-n}$  between this peak and larger wave numbers (corresponding to smaller scales). We computed  $n$  (the slope of the spectra) for each model snapshot (Figure 16). The value  $n$  characterizes the spatial distribution of the quantity examined. It indicates whether the small-scale structures are energetic (small  $n$ ) or not (large  $n$ ).

[58] During the first 15 days of the experiment, the slope of SST, MLD, surface relative vorticity (RV) and nitrate rapidly decreases. This corresponds to an adjustment period during which the small scales, that were absent in the rather smooth initial fields, are progressively generated by the flow. This is not the case for phytoplankton and zooplankton which are homogeneously initialized. They start with a rather flat slope because small-scale noise is generated during the first few days of the adjustment. The slope of SST (−2) and RV (−1) are close to the theoretical values [*Klein et al.*, 1998; *Lévy and Klein*, 2004]. The MLD slope is close to −1 during periods of deep MLDs, and close to −2 when the water column is more stratified. Similar MLD's slopes were calculated by *Paci et al.* [2005] with 1-D FFTs. The MLD filaments are naturally more energetic

**Table A4.** Optical Parameters

Symbol	Value	Unit
$k_{r0}$	0.225	$m^{-1}$
$k_{b0}$	0.0232	$m^{-1}$
$\chi_{rp}$	0.037	$m^{-1}(mgChl\ m^{-3})^{-e_r}$
$\chi_{bp}$	0.074	$m^{-1}(mgChl\ m^{-3})^{-e_b}$
$e_r$	0.629	
$e_b$	0.674	
$r_{pig}$	0.7	

**Table A5.** Remineralization Equations Below the Euphotic Layer

Description	Equation	
Nitrate source/sink	$S(\text{NO}_3) = \tau_r(\text{NH}_4 + P + Z + D + \text{DOM}) + \partial_z f$	(23)
Ammonium source/sink	$S(\text{NH}_4) = -\tau_r \text{NH}_4$	(24)
Phytoplankton source/sink	$S(P) = -\tau_r P$	(25)
Zooplankton source/sink	$S(Z) = -\tau_r Z$	(26)
Detritus source/sink	$S(D) = -\tau_r D - V_d \partial_z D$	(27)
DOM source/sink	$S(\text{DOM}) = -\tau_r \text{DOM}$	(28)
Remineralization flux	$f(z) = f(z_{\text{bio}}) \left( \frac{z}{z_{\text{bio}}} \right)^{-r}$	(29)
Instantaneous export	$f(z_{\text{bio}}) = \int_0^{z_{\text{bio}}} (1 - f_z) m_z Z^2 dz$	(30)
No floor deposition	$f(z_{\text{bottom}}) = 0.0$	(31)

in the presence of large MLD gradients. Until mid-May, nitrate has the same large-scale structure as SST and a comparable spectrum slope. The spectrum slopes for phytoplankton and zooplankton are more temporally variable. During the onset of the bloom, phytoplankton is forced at small scales by the small scales of the MLD. The slope of phytoplankton progressively increases during and after the bloom, reaching the value of the nitrate slope by mid-April. This highlights the transition from a light-controlled regime, with very energetic small scales, to a nutrient controlled regime, with less energetic small scales. Zooplankton follows this change of regime, but with a 1 month delay. A third regime is expected to occur during oligotrophic conditions, with much flatter slopes for both nitrate and phytoplankton [Lévy *et al.*, 2001]. After mid-May, when nutrients are nearly exhausted at the surface, this switch of regime can be seen in the rapid decrease of the nutrient slope, but not yet in the slope of phytoplankton. A study dedicated to POMME 3 (August–September 2001) should provide more insight on this summer regime. Moreover, work is in progress to examine the change of spectral slopes predicted by the model with high-resolution SeaWiFS images. Regarding data analysis, these results suggest that phytoplankton submesoscale features should be much more visible during P1 than during P2.

## 6. Summary and Conclusions

[59] A high-resolution physical-biological regional ocean model forced with high (spatiotemporal) resolution atmospheric fluxes was used to simulate the characteristics of the spring bloom during the POMME experiment. The model was successfully calibrated to fit the observations, except in late spring during a storm, because the resulting vertical mixing in the model was not as active as the observed one. The model was used to simulate the evolution of the 2001 bloom, from February until May, between 38°N and 45°N.

[60] This reconstruction enabled to emphasize and to explain the unusual characteristics of this bloom. Its quite long duration (2 months) and low intensity ( $1 \text{ mgChl m}^{-3}$ ), are enabled by a slow stratification, intermittent nutrient

reloading, and a strong coupling between phytoplankton and zooplankton. The low  $f$ -ratio (0.45) can only be obtained with a large source of regeneration (DOM). It is associated with a very small  $e$ -ratio (0.05), suggesting a winter export of DOM.

[61] Moreover, the variability revealed by the model appeared to be much higher than that evidenced in the data. This large variability is essentially driven by the variability of the atmospheric forcing. On the seasonal timescale, NP increases by a factor two between winter and spring. Short-term time variability in buoyancy, wind, and solar radiation can change NP by a factor two over periods of 3–4 days, and over regions of 1–2° wide. Another factor driving variability is the stirring induced by the mesoscale eddies. An original result of this study is the initiation of the bloom in specific submesoscale structures (10 km by 100 km), which are filaments of shallower MLD. Later in the season, filaments transport nutrients from the north to the south. The small-scale time variability (of atmospheric origin) and space variability (of oceanic origin) have comparable magnitudes. This study suggests that both high-resolution of the model grid and high resolution of the atmospheric forcings are necessary to capture the small-scale (1–8 days, 10–100 km) variability in the ocean. This variability is such that it cannot be sampled at sea, even with the means deployed during POMME.

[62] The analysis of the variability in the model, with regards to the data coverage of POMME, has then been used as a framework to evaluate the representativeness of the observed variability. The main conclusions of this analysis is that it is reasonable to derive seasonal budgets from the data sets, but that it is hazardous to analyze the space variability of the leg 1 arrays, or of the leg 2 time series stations, without carefully taking into account the asynopticity of the observations.

[63] In order to fulfill the objectives of POMME, a number of questions deserve to be further addressed, such as the origin of the high regenerated production, the role of zooplankton and of the winter preconditioning, the variability of the carbon and oxygen, and, concerning the dynamics, the validation of the vertical velocities. Work is in

**Table A6.** Remineralization Parameters

Parameter Name	Symbol	Value	Unit
Depth of euphotic layer	$z_{\text{bio}}$	150	m
Bottom topography	$z_{\text{bottom}}$	variable	m
Remineralization rate at depth	$\tau_r$	$5.80 \times 10^{-7}$	$\text{s}^{-1}$
Exponential decay	$r$	0.858	

progress, and simulations using a more complete biological model (S. Roudesli et al., personal communication, 2004) and over a complete seasonal cycle [Giordani et al., 2005] are part of ongoing research.

### Appendix A: Lodyc Ocean Biogeochemical Simulation Tools for Ecosystem and Resources (LOBSTER) Biological Model

[64] The Lodyc Ocean Biogeochemical Simulation Tools for Ecosystem and Resources (LOBSTER) model (Figure A1) consists of six prognostic variables expressed in terms of their nitrogen content: nitrate ( $\text{NO}_3$ ), ammonium ( $\text{NH}_4$ ), phytoplankton ( $P$ ), zooplankton ( $Z$ ), detritus ( $D$ ) and semilabile dissolved organic matter (DOM). Each of these tracer  $C$  is freely advected and diffused by the flow, and is submitted to a specific source/sink term  $S(C)$  which describes the biogeochemical interactions among the tracers (Table A1, equation (1)). The biogeochemical model in the euphotic layer is described by equations in Table A1, with parameter values in Table A2. The photosynthetic available radiation (PAR) is computed from a two wavelength light absorption model (Tables A3 and A4). Below the euphotic layer, remineralization is described by the equations in Table A5 and parameters in Table A6. The bottom of the euphotic layer is treated as a constant depth (150 m).

[65] The processes accounted for in the euphotic layer model are advection ( $-\nabla(\mathbf{u}C)$ ), vertical diffusion ( $(\partial/\partial z)(k_z(\partial C/\partial z))$ ) and lateral diffusion ( $D_{\text{lat}}$ ) of all state variables, phytoplankton growth on nitrate ( $\mu_p L_I L_{\text{NO}_3} P$ ), phytoplankton growth on ammonium ( $\mu_p L_I L_{\text{NH}_4} P$ ), phytoplankton mortality ( $m_p P$ ), grazing of phytoplankton ( $G_p$ ), grazing of detritus ( $G_d$ ), fecal pellets production ( $(1 - a_z)(G_p + G_d)$ ), nitrification ( $\mu_n \text{NH}_4$ ), exudation ( $\gamma \mu_p L_I (L_{\text{NO}_3} + L_{\text{NH}_4}) P$ ), quadratic zooplankton mortality ( $m_z Z^2$ ), zooplankton excretion ( $\mu_z Z$ ), detritus breakdown ( $\mu_d D$ ), DOM remineralization ( $\mu_{\text{dom}} \text{DOM}$ ), and sinking of detritus ( $V_d \partial_z D$ ). Photoadaptation ( $R_{\text{Chl:N}}$ ) is a function of the daily PAR ( $\overline{\text{PAR}}$ ). The light absorption model is forced by the incoming solar radiation ( $Q_{\text{sol}}$ ). Remineralization below the euphotic layer is simply parameterized as a linear decay of all state variables eventually feeding the nitrate compartment ( $\tau_r(\text{NH}_4 + P + Z + D + \text{DOM})$ ). In LOBSTER, fast sinking detritus can be parameterized by a fraction of the zooplankton mortality flux that instantaneously feeds the aphotic layer ( $(1 - f_z)m_z Z^2$ ). This option is not activated in this study in order to fit the observed  $e$ -ratio ( $f_z = 1$ ). In consequence, the zooplankton mortality flux is entirely directed toward the slow sinking detritus.

[66] **Acknowledgments.** This work is a contribution to the POMME program. Financial support was provided by the French agencies CNRS, IFRÉMER, Meteo-France, and SHOM. The data synthesis presented in this study results from a joint effort by all POMME participants. The model setup and analysis were funded by grants from the French research program PROOF. We are grateful to Andreas Oschlies and two anonymous reviewers for their help in improving the original form of this manuscript and to Carroll Susco for her help in latex editing.

### References

Anderson, L. A., and A. R. Robinson (2001), Physical and biological modeling in the Gulf Stream region: Part II. Physical and biological processes, *Deep Sea Res., Part I*, 48, 1139–1168.

- Assenbaum, M., and G. Reverdin (2005), Near real-time analyses of the mesoscale circulation during the POMME experiment, *Deep Sea Res., Part I*, in press.
- Bender, M., H. Ducklow, J. Kiddon, J. Marra, and J. Martin (1992), The carbon balance during the 1989 spring bloom in the North Atlantic Ocean, 47°N, 20°W, *Deep Sea Res., Part A*, 39, 1707–1725.
- Blain, S., C. Guieu, H. Claustre, K. Leblanc, T. Moutin, B. Quéguiner, J. Ras, and G. Sarthou (2004), Availability of iron for phytoplankton in the north-east Atlantic Ocean, *Limnol. Oceanogr.*, 49, 2095–2104.
- Blayo, E., J. Verron, and J. M. Molines (1994), Assimilation of TOPEX/POSEIDON altimeter data into a circulation model of the North Atlantic, *J. Geophys. Res.*, 99, 24,691–24,705.
- Bourras, D., G. Reverdin, H. Giordani, and G. Caniaux (2004), Response of the atmospheric boundary layer to a mesoscale oceanic eddy in the northeast Atlantic, *J. Geophys. Res.*, 109, D18114, doi:10.1029/2004JD004799.
- Bury, S. J., P. W. Boyd, T. Preston, G. Savidge, and N. J. P. Owens (2001), Size-fractionated primary production and nitrogen uptake during a North Atlantic phytoplankton bloom: Implications for carbon export estimates, *Deep Sea Res., Part I*, 48, 689–720.
- Caniaux, G., A. Brut, D. Bourras, H. Giordani, A. Paci, L. Prieur, and G. Reverdin (2005), A 1 year sea surface heat budget in the north-eastern Atlantic basin during the POMME experiment: 1. Flux estimates, *J. Geophys. Res.*, doi:10.1029/2004JC002596, in press.
- Claustre, H., M. Babin, D. Merien, J. Ras, L. Prieur, S. Dallot, O. Prasil, H. Dousova, and T. Moutin (2005), Toward a taxon-specific parameterization of bio-optical models of primary production: A case study in the North Atlantic, *J. Geophys. Res.*, doi:10.1029/2004JC002634, in press.
- Fernandez, C. I., P. Raimbault, N. Garcia, P. Rimmelin, and G. Caniaux (2005a), An estimate of annual new production and carbon fluxes in the northeast Atlantic Ocean during 2001, *J. Geophys. Res.*, doi:10.1029/2004JC002616, in press.
- Fernandez, C. I., P. Raimbault, G. Caniaux, N. Garcia, and P. Rimmelin (2005b), Influence of the mesoscale eddies on nitrate distribution during the POMME program in the northeast Atlantic Ocean, *J. Mar. Syst.*, 55, 155–175.
- Franks, P. J. S., and C. Chen (2001), A 3-D prognostic numerical model study of the Georges bank ecosystem. Part II: Biological-physical model, *Deep Sea Res., Part II*, 48, 457–482.
- Garside, C., and J. C. Garside (1993), The “f-ratio” on 20°W during the North Atlantic Bloom Experiment, *Deep Sea Res., Part II*, 40, 75–90.
- Gaspar, P., Y. Gregoris, and J.-M. Lefevre (1990), A simple eddy-kinetic-energy model for simulations of the oceanic vertical mixing: Tests at station Papa and Lotus site, *J. Geophys. Res.*, 95, 16,179–16,193.
- Gavart, M., P. De Mey, and G. Caniaux (1999), Assimilation of satellite altimeter data in a primitive-equation model of the Azores-Madeira region, *Dyn. Atmos. Oceans*, 29, 217–254.
- Giordani, H., G. Caniaux, L. Prieur, A. Paci, and S. Giraud (2005), A 1 year mesoscale simulation in the northeast Atlantic: Mixed layer heat and detrainment budgets during the POMME experiment, *J. Geophys. Res.*, doi:10.1029/2004JC002765, in press.
- Guieu, C., M. Roy-Barman, N. Leblond, C. Jeandel, M. Souhant, B. Le Cann, A. Dufour, and C. Bourmot (2005), Vertical particle flux in the northeast Atlantic Ocean (POMME experiment), *J. Geophys. Res.*, doi:10.1029/2004JC002672, in press.
- Harrison, W. G., E. J. H. Head, E. P. W. Horne, B. Irwin, W. K. W. Li, A. R. Longhurst, M. A. Paranjape, and T. Platt (1993), The western North Atlantic bloom experiment, *Deep Sea Res., Part II*, 40, 279–305.
- Hazeleger, W., and S. S. Drijfhout (2000), Eddy subduction in a model of the subtropical gyre, *J. Phys. Oceanogr.*, 30, 677–695.
- Jenkins, W. J. (1998), Studying subtropical thermocline ventilation and circulation using tritium and  $^3\text{He}$ , *J. Geophys. Res.*, 103, 15,817–15,831.
- Karayanni, H., U. Christaki, F. Van Wambeke, and A. P. Dalby (2005a), Evaluation of double formalin–Lugol’s fixation in assessing number and biomass of ciliates: An example of estimations at mesoscale in NE Atlantic, *J. Microbiol. Methods*, in press.
- Karayanni, H., U. Christaki, F. Van Wambeke, M. Denis, and T. Moutin (2005b), Influence of ciliated protozoa and heterotrophic nanoflagellates on the fate of primary production in the northeast Atlantic Ocean, *J. Geophys. Res.*, 110, C07S15, doi:10.1029/2004JC002602.
- Klein, P., A.-M. Triguier, and L. Hua (1998), Three-dimensional stirring of thermohaline fronts, *J. Mar. Res.*, 56, 589–612.
- Kortzinger, A., W. Koeve, P. Kahler, and L. Mintrop (2001), C:N ratios in the mixed layer during the productive season in the northeast Atlantic Ocean, *Deep Sea Res., Part I*, 48, 661–688.
- Leblanc, K., A. Leynaert, I. C. Fernandez, P. Rimmelin, T. Moutin, P. Raimbault, J. Ras, and B. Queguiner (2005), A seasonal study of diatom dynamics in the North Atlantic during the POMME experiment (2001): Evidence for Si limitation of the spring bloom, *J. Geophys. Res.*, doi:10.1029/2004JC002621, in press.

- Lévy, M., and P. Klein (2004), Does the low frequency variability of mesoscale dynamics explain a part of the phytoplankton and zooplankton spectral variability?, *Proc. R. Soc. London*, *460*, 1673–1688.
- Lévy, M., L. Mémerly, and J.-M. André (1998), Simulation of primary production and export fluxes in the NW Mediterranean Sea, *J. Mar. Res.*, *56*, 197–238.
- Lévy, M., L. Mémerly, and G. Madec (2000), The onset of a bloom in the MEDOC area: Mesoscale and high-frequency spatial variability, *Deep Sea Res. Part I*, *47*, 27–53, doi:10.1016/S0967-0637(99)00051-5.
- Lévy, M., P. Klein, and A.-M. Treguier (2001), Impacts of sub-mesoscale physics on phytoplankton production and subduction, *J. Mar. Res.*, *59*, 535–565.
- Lévy, M., Y. Lehahn, J.-M. André, L. Mémerly, H. Loisel, and E. Heifetz (2005), Production regimes in the northeast Atlantic: A study based on Sea-viewing Wide Field-of-view Sensor chlorophyll and ocean general circulation model mixed layer depth, *J. Geophys. Res.*, doi:10.1029/2004JC002771, in press.
- Lochte, K., H. W. Ducklow, M. J. R. Fasham, and C. Stienen (1993), Plankton succession and carbon cycling at 47°N 20°W during the JGOFS North Atlantic Bloom Experiment, *Deep Sea Res., Part II*, *40*, 91–114.
- Madec, G., P. Delecluse, M. Imbard, and C. Lévy (1999), OPA 8.1 ocean general circulation model reference manual, Note du Pole de Modelisation, Inst. Pierre-Simon Laplace, Paris.
- Mahadevan, A., and D. Archer (2000), Modeling the impact of fronts and mesoscale circulation on the nutrient supply and biogeochemistry of the upper ocean, *J. Geophys. Res.*, *105*, 1209–1225.
- Maixandeau, A., et al. (2005), Microbial community production, respiration, and structure of the microbial food web of an ecosystem in the north-eastern Atlantic Ocean, *J. Geophys. Res.*, doi:10.1029/2004JC002694, in press.
- McCartney, M. S., and L. D. Talley (1982), The subpolar Mode Water in the North Atlantic Ocean, *J. Phys. Oceanogr.*, *12*, 1169–1188.
- McGillicuddy, D. J., Jr., J. J. McCarthy, and A. R. Robinson (1995a), Coupled physical and biological modeling of the spring bloom in the North Atlantic (I): Model formulation and one dimensional bloom processes, *Deep Sea Res., Part I*, *42*, 1313–1357.
- McGillicuddy, D. J., Jr., A. R. Robinson, and J. J. McCarthy (1995b), Coupled physical and biological modeling of the spring bloom in the North Atlantic (II): Three dimensional bloom and post-bloom processes, *Deep Sea Res., Part I*, *42*, 1359–1398.
- McGillicuddy, D. J., Jr., A. R. Robinson, D. A. Siegel, H. W. Jannasch, R. Johnson, T. D. Dickey, J. McNeil, A. F. Michaels, and A. H. Knap (1998), Influence of mesoscale eddies on new production in the Sargasso Sea, *Nature*, *394*, 263–265.
- McGillicuddy, D. J., Jr., D. R. Lynch, P. Wiebe, J. Runge, E. G. Durbin, W. C. Gentleman, and C. S. Davis (2001), Evaluating the synopticity of the US GLOBEC Georges Bank broad-scale sampling pattern with observational system simulation experiments, *Deep Sea Res., Part II*, *48*, 483–499.
- Mellor, G., and A. Blumberg (2004), Wave breaking and ocean surface layer thermal response, *J. Phys. Oceanogr.*, *34*, 693–698.
- Mémerly, L., G. Reverdin, J. Paillet, and A. Oschlies (2005), Introduction to the POMME special section: Thermocline ventilation and biogeochemical tracer distribution in the northeast Atlantic Ocean and impact of mesoscale dynamics, *J. Geophys. Res.*, doi:10.1029/2005JC002976, in press.
- Oschlies, A., and V. Garçon (1998), Eddy-induced enhancement of primary production in a model of the North Atlantic Ocean, *Nature*, *394*, 266–269.
- Paci, A., G. Caniaux, M. Gavart, H. Giordani, M. Lévy, L. Prieur, and G. Reverdin (2005), A high-resolution simulation of the ocean during the POMME experiment: 1. Simulation results and comparison with observations, *J. Geophys. Res.*, doi:10.1029/2004JC002712, in press.
- Paillet, J., and M. Arhan (1996a), Shallow pycnoclines and mode water subduction in the eastern North Atlantic, *J. Phys. Oceanogr.*, *26*, 96–114.
- Paillet, J., and M. Arhan (1996b), Oceanic ventilation in the eastern North Atlantic, *J. Phys. Oceanogr.*, *26*, 2036–2052.
- Pollard, R. T., and L. A. Regier (1992), Vorticity and vertical circulation at an ocean front, *J. Phys. Oceanogr.*, *22*, 609–625.
- Popova, E. E., C. J. Lozano, M. A. Srokosz, M. J. R. Fasham, P. J. Haley, and A. R. Robinson (2002), Coupled 3D physical and biological modeling of the mesoscale variability observed in northeast Atlantic in spring 1997: Biological processes, *Deep Sea Res., Part I*, *49*, 1741–1768.
- Rios, A. F., T. R. Anderson, and F. F. Perez (1995), The carbonic system distribution and fluxes in the NE Atlantic during spring 1991, *Prog. Oceanogr.*, *35*, 295–314.
- Robinson, A., et al. (1993), Mesoscale and upper ocean variabilities during the 1989 JGOFS bloom study, *Deep Sea Res., Part II*, *40*, 9–35.
- Sieracki, M. E., P. G. Verity, and D. K. Stoecker (1993), Plankton community response to sequential silicate and nitrate depletion during the 1989 North Atlantic spring bloom, *Deep Sea Res., Part II*, *40*, 213–225.
- Valdivieso da Costa, M., H. Mercier, and A.-M. Treguier (2005), Effects of the mixed-layer time variability on kinematic subduction rate diagnostics, *J. Phys. Oceanogr.*, in press.
- Vialard, J., and P. Delecluse (1998), An OGCM study for the TOGA decade. part I: Role of salinity in the physics of the western Pacific fresh pool, *J. Phys. Oceanogr.*, *6*, 1071–1088.
- Williams, R. G., and M. J. Follows (1998), The Ekman transfer of nutrients and maintenance of new production over the North Atlantic, *Deep Sea Res., Part I*, *45*, 461–489.
- Williams, R. G., and M. J. Follows (2003), Physical transport of nutrients and the maintenance of biological production, in *Ocean Biogeochemistry: The Role of the Ocean Carbon Cycle in Global Change*, edited by M. Fasham, pp. 19–51, Springer, New York.
- Yoder, J. A., J. Aiken, R. N. Swift, F. E. Hoge, and P. M. Stegman (1993), Spatial variability in near-surface chlorophyll: A fluorescence measured by the Airborne Oceanographic Lidar (AOL), *Deep Sea Res., Part II*, *40*, 37–53.

G. Caniaux and A. Paci, Centre National de Recherches Meteorologiques, Météo-France, 42, av G. Coriolis, F-31057 Toulouse, France. (guy.caniaux@meteo.fr; alexandre.paci@meteo.fr)

M. Gavart, Service Hydrographique et Océanographique de la Marine, 14 avenue E. Belin, F-31400 Toulouse, France. (gavart-consultant@wanadoo.fr)

M. Lévy, Laboratoire d'Océanographie Dynamique et de Climatologie/ Institut Pierre-Simon Laplace, Université Pierre et Marie Curie, BC100, 4, place Jussieu, F-75252 Paris Cedex 05, France. (marina@lodyc.jussieu.fr)

L. Mémerly, Laboratoire des Sciences de l'Environnement Marin, CNRS, UMR 6539, Institut Universitaire Européen de la Mer, Technopole Brest Iroise, F-29280 Plouzané, France. (memery@lodyc.jussieu.fr)

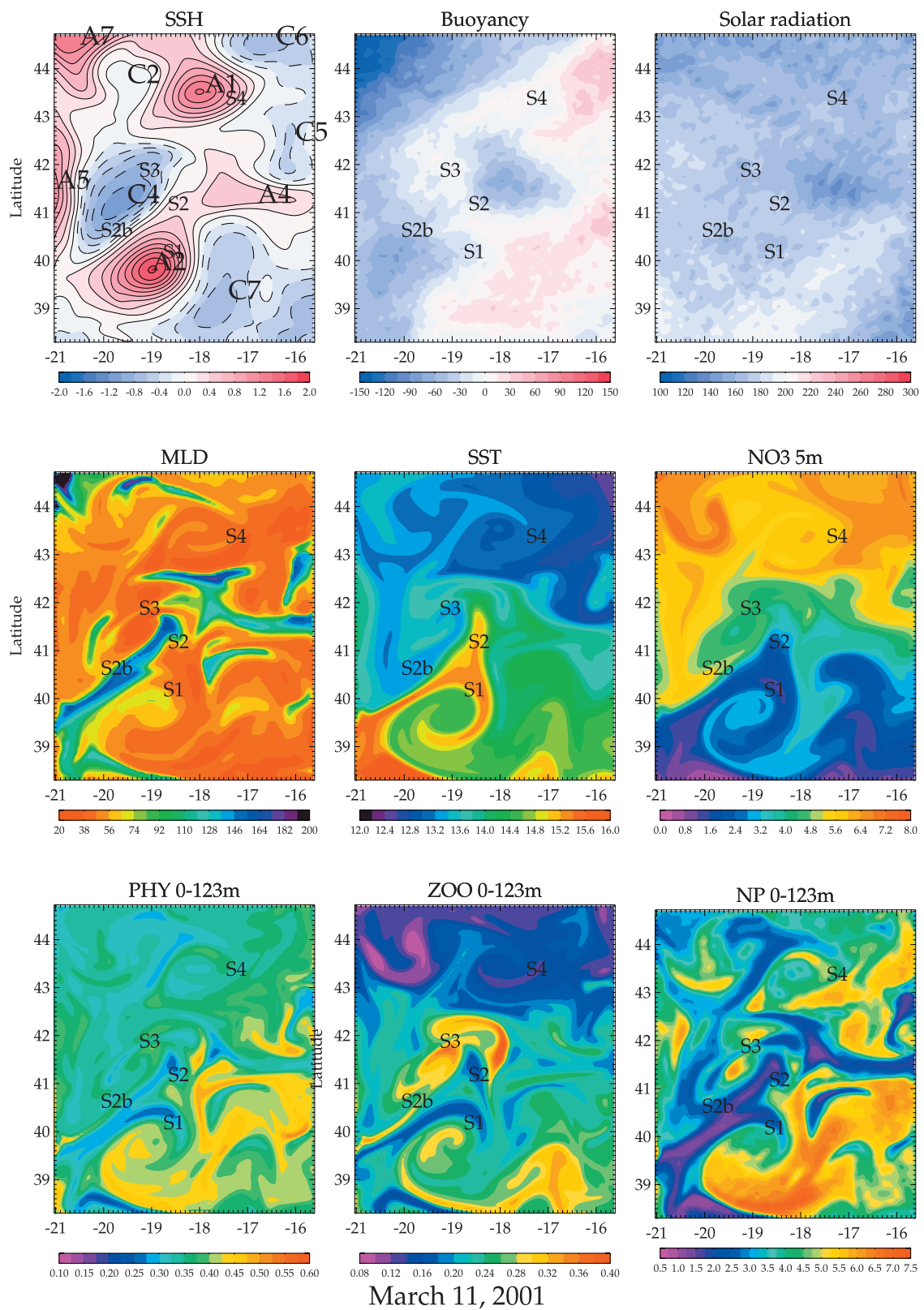


**Figure 8.** Snapshots of model outputs during P1L2 (11 March 2001). Also indicated are the locations of the time series stations.

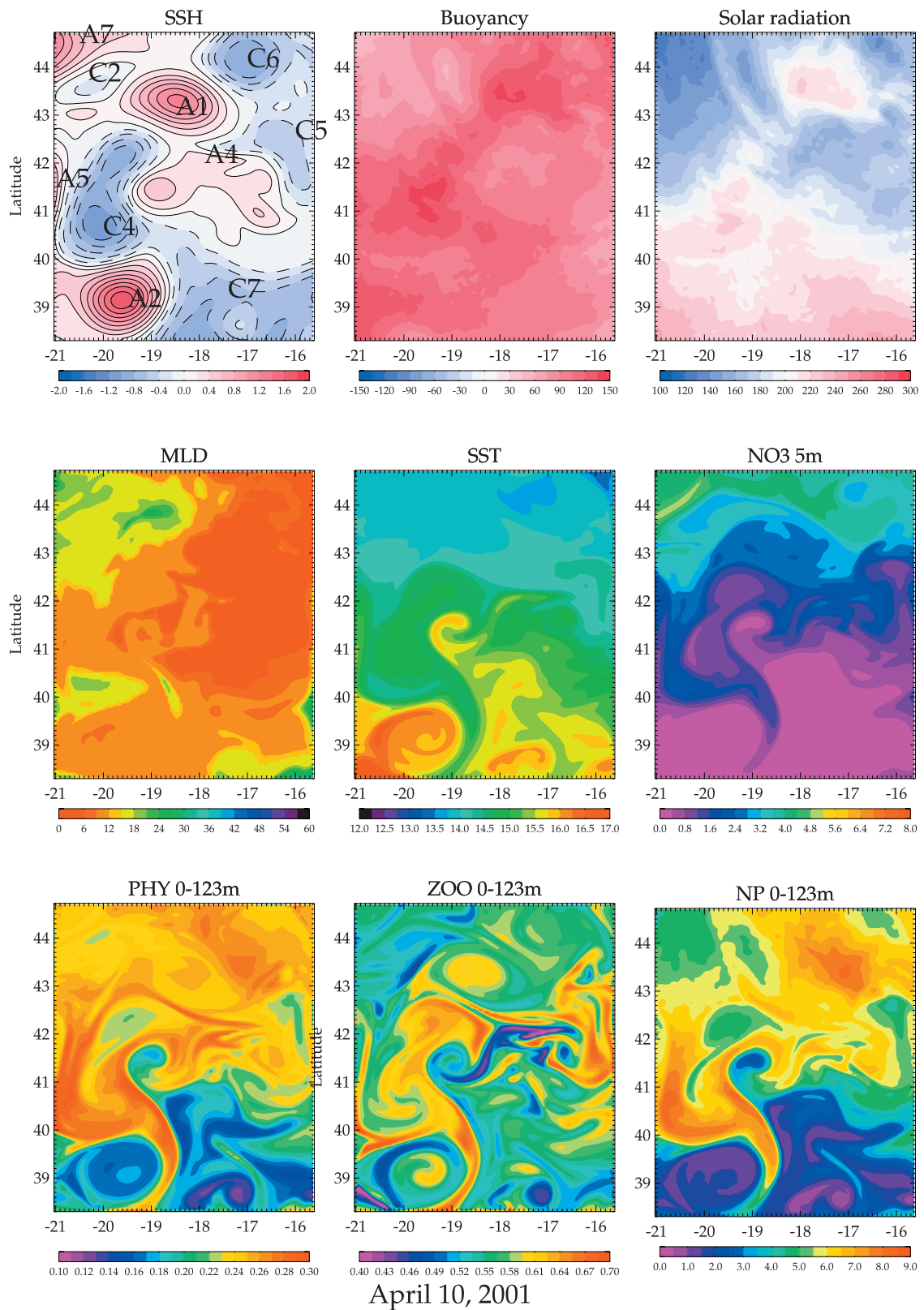


**Figure 9.** Snapshots of model outputs during P2L1 (10 April 2001). Note that the color scales are not always the same as in Figure 8.

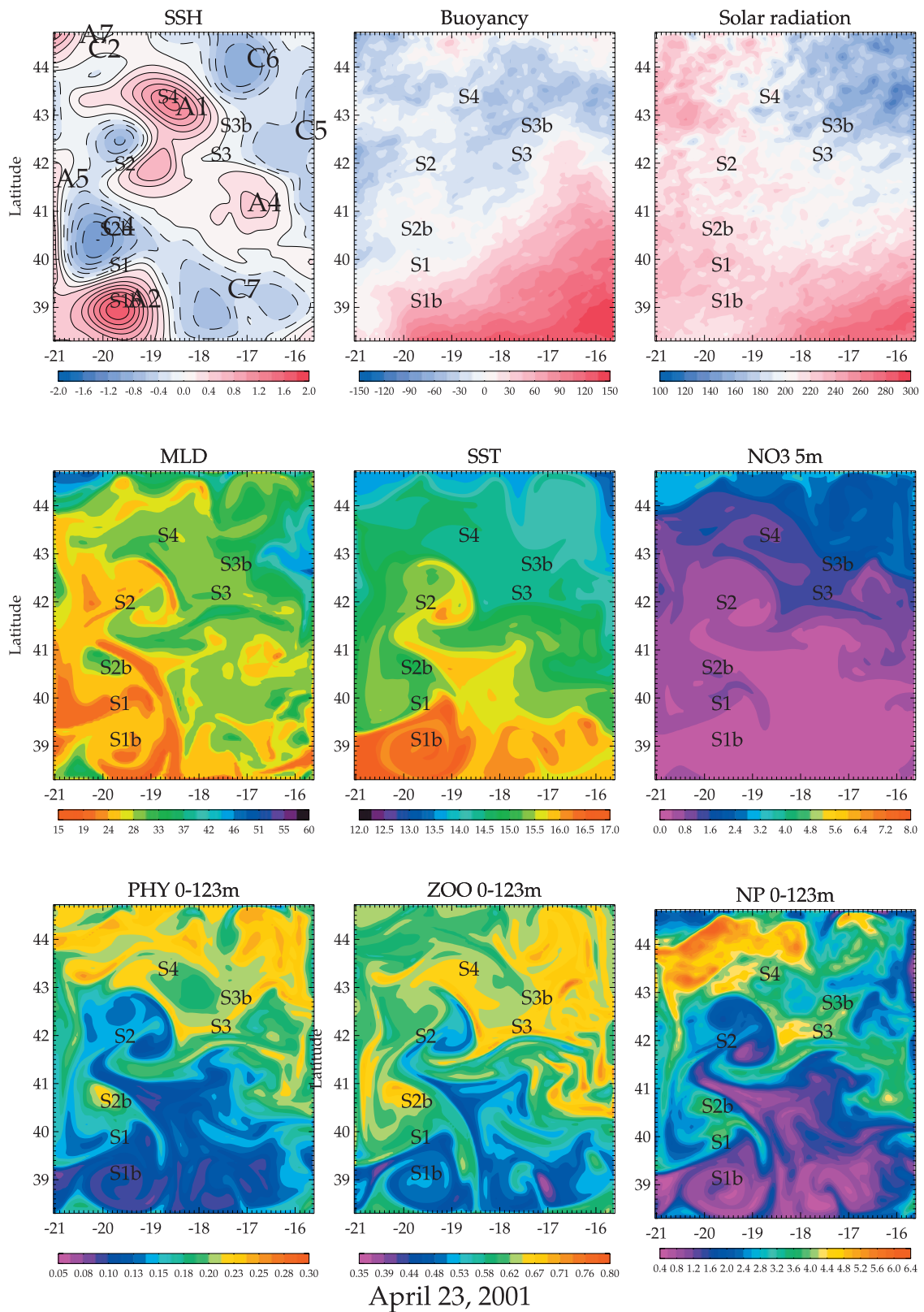


**Figure 10.** Snapshots of model outputs during P2L2 (23 April 2001). Note that the color scales are not always the same as in Figures 8 and 9. Also indicated are the location of the time series stations.

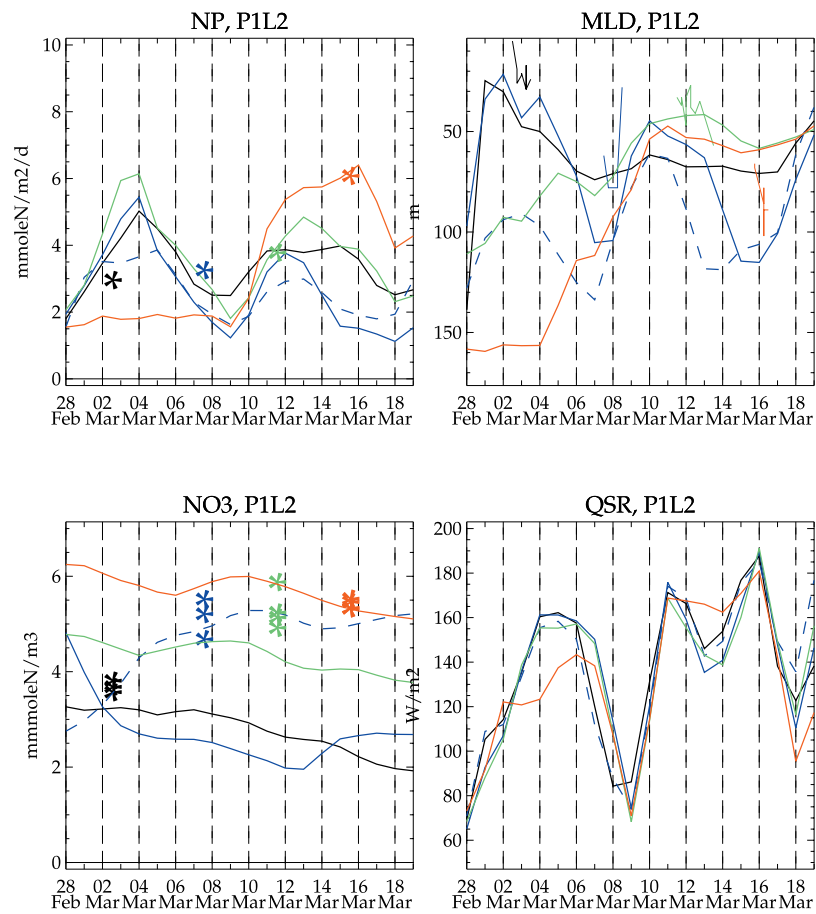


**Figure 13.** Time evolution during P1L2 of the model new production (NP), mixed layer depth (MLD), surface nitrate concentration ( $\text{NO}_3$ ), and solar radiation (QSR) at stations S1 (black), S2 (blue), S2b (dashed blue), S3 (green), and S4 (red), compared with the observations (asterisks for surface nitrate and NP, thin lines for MLD time series).

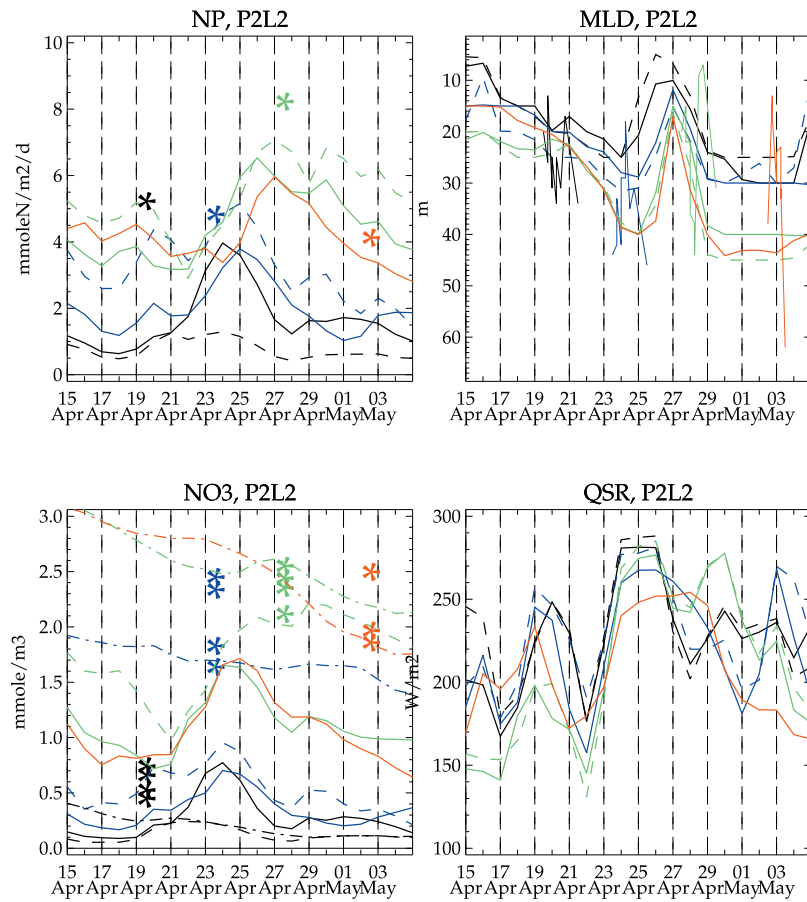


**Figure 15.** Time evolution during P2L2 of the model new production, mixed layer depth, surface nitrate concentration, and solar radiation at stations S1 (black), S1b (dashed black), S2 (blue), S2b (dashed blue), S3 (green), S3b (dashed green), and S4 (red) compared with the observations (asterisks for surface nitrate and NP, thin lines for MLD time series). Nitrate concentration at the observed mixed layer depth and at stations S1, S2b, S3b, and S4 are shown with dash-dotted lines.